Monthly Notices
of the
ROYAL ASTRONOMICAL SOCIETY

MNRAS **552,** 1–18 (2026) https://doi.org/10.1093/mnras/stag1595
Advance Access publication 2026 August 22

# Earliest simultaneous multicolour optical observations of GRB 230328B: from 41 s to the host-galaxy identification

T. Komesh [1,2,3★] A. Pozanenko,[4,5★] N. Pankov,[4,5] A. Volnova,[4] P. Minaev [4] R. Gill,[6,7] D. Berdikhan,[1] B. Grossan,[1,8†] Z. Maksut,[1] Z. Abdullayev,[9,10] S. Belkin [11] M. Krugov,[12] A. Moskvitin,[13] K. Baigarin,[1] A. Tursynkan,[14] E. Klunko,[15] A. Tatarnikov,[16] S. Zheltoukhov,[16] V. Rumyantsev,[17] A. Volvach,[17] L. Volvach,[17] O. A. Burkhonov [18] S.A. Ehgamberdiev,[18,19] R. Inasaridze,[20,21] L. Elenin,[22] A. Krylov,[22] M. Zheltobryukhov,[23] S. B. Pandey,[24] A. K. Ror [24] R. Gupta,[25‡] V. Swain,[26] V. Bhalerao,[26] G. C. Anupama [27] S. Barway [27] R. Sánchez-Ramírez,[28] A. J. Castro-Tirado,[28] S. Antier [29,30] P. Beniamini[7,31,32] and E. Abdikamalov [1,14]

*Affiliations are listed at the end of the paper*

Accepted 2026 August 20. Received 2026 August 5; in original form 2026 May 28

## ABSTRACT

We present a multiwavelength study of the long-duration gamma-ray burst GRB 230328B, combining prompt $\gamma$-ray observations with exceptionally early simultaneous optical photometry and extensive X-ray, radio, and host-galaxy follow-up. NUTTELA-TAO began simultaneous $g'r'i'$ observations only 41 s after the *Swift*/BAT trigger, corresponding to approximately 16 s in the rest frame for the adopted host-galaxy photometric redshift of $z_{\mathrm{phot}} = 1.54 \pm 0.06$. Unlike sequential multiband measurements, these observations provide an instantaneous optical spectral slope without temporal-interpolation uncertainties. The early optical continuum remains statistically consistent with a constant slope from approximately $10^2$ to $7 \times 10^3$ s, providing no evidence for rapid dust destruction. The absence of significant colour evolution across the pronounced optical rebrightening at approximately $4 \times 10^3$ s demonstrates that it is achromatic and favours a dynamical rather than spectral origin. Broad-band modelling shows that the optical, X-ray, and radio evolution can be broadly explained by forward-shock emission with late energy injection, although alternative scenarios cannot be excluded. The red optical continuum is consistent with substantial line-of-sight extinction in a massive, dusty host galaxy. Late-time observations are insufficient to constrain a typical GRB-associated supernova at the adopted redshift. GRB 230328B therefore provides a benchmark for connecting the earliest simultaneous optical colours with afterglow dynamics and the host environment of a representative long GRB.

**Key words:** methods: observational – gamma-ray burst: individual: GRB 230328B – galaxies: distances and redshifts – gamma-ray bursts.

## 1 INTRODUCTION

Gamma-ray bursts (GRBs) are energetic explosions driven by relativistic jets. They are characterized by a *prompt* phase, which emits $\gamma$-rays due to internal dissipation within the jet. This is followed by a broad-band *afterglow*, spanning X-rays to radio frequencies, generated as the jet interacts with the ambient medium (e.g. T. Piran 1999; P. Kumar & B. Zhang 2015). Beyond probing relativistic jet dynamics, particle acceleration (e.g. L. Sironi & A. Spitkovsky 2011), and jet structure (P. Beniamini & E. Nakar 2019; B. O'Connor et al. 2023), GRBs also serve as powerful probes of star formation, metal enrichment, and the interstellar and intergalactic media across a wide redshift range (e.g. J. T. Palmerio et al. 2019; R. Gupta et al. 2022; J. F. Graham, P. Schady & A. S. Fruchter 2023). Despite decades of progress, key questions about the nature of GRBs remain, including the physical mechanism responsible for the prompt $\gamma$-ray emission, the composition and energy-dissipation processes of the relativistic jet, the structure and density profile of the circumburst environment, and the connection between GRB progenitors and their host-galaxy environments (e.g. P. Kumar & B. Zhang 2015; A. S. Pozanenko et al. 2021). Addressing these questions motivates coordinated multiwavelength observations from the earliest phases of the burst through the late afterglow and host-galaxy identification.

★ E-mail: toktarkhan.komesh@nu.edu.kz (TK); apozanen@iki.rssi.ru (AP)
† Deceased.
‡ NASA Post-doctoral Program Fellow.

GRB durations exhibit a bimodal distribution (C. Kouveliotou et al. 1993). Bursts with $T_{90} \leq 2$ s, where $T_{90}$ is the interval over which 90 per cent of the prompt $\gamma$-ray fluence is detected, are classified as short, while those with $T_{90} > 2$ s are classified as long (E. P. Mazets et al. 1981; B. Zhang 2025). Since short and long GRBs tend to exhibit harder and softer spectra, they are commonly referred to as short-hard (Type I) and long-soft (Type II) bursts (B. Zhang 2006; B. Zhang et al. 2009). This divide is largely tied to distinct progenitors. The short GRB 170817A, detected in coincidence with a gravitational wave signal and a subsequent kilonova, confirmed a binary neutron star merger origin for Type I events (B. P. Abbott et al. 2017). Long GRBs are associated with core-collapse supernovae (SNe; e.g. S. E. Woosley 1993; G. Finneran, L. Cotter & A. Martin-Carrillo 2025). Examples include the associations of GRB 980425/SN 1998bw (T. J. Galama et al. 1998) and GRB 030329/SN 2003dh (J. Hjorth et al. 2003). However, this duration-based classification is not absolute (B. Zhang 2025). For example, GRB 211211A exhibited a duration of $T_{90} > 2$ s but showed clear kilonova signatures, indicating a merger origin despite its extended emission (E. Troja et al. 2022).

GRB afterglows are powerful tools for studying GRBs and their surroundings. The afterglow is governed by both intrinsic burst parameters (e.g. H. Gao et al. 2013) and the properties of the ambient medium (E.-W. Liang et al. 2013; X. Tian et al. 2022). The afterglow signal can differentiate between a stellar wind profile and interstellar medium (ISM) (R. A. Chevalier & Z.-Y. Li 1999), and reveal transitions between the two, as seen in GRB 140423A (L. Li et al. 2020) and GRB 160625B (N. Fraija et al. 2017). D. Lazzati et al. (2006) utilized time-resolved spectroscopy to uncover a clumpy, extended wind environment around GRB 021004, highlighting the necessity of high-quality, wide-time-scale multicolour data. GRBs act as bright 'backlights' for their host galaxies (B. T. Draine & L. Hao 2002; Y. Li, A. Li & D. M. Wei 2008). Dust extinction in the ISM leaves a distinct imprint on the optical-ultraviolet (UV) spectrum of the burst (D. A. Kann, S. Klose & A. Zeh 2006; P. Schady et al. 2010; A. Melandri et al. 2017; L. Li et al. 2018). Several studies have reported colour evolution from red to blue on short ($\sim 10^3$ s) time-scales, consistent with dust destruction by the UV/X-ray radiation of the GRB (R. Perna, D. Lazzati & F. Fiore 2003; A. N. Morgan et al. 2014; T. Komesh et al. 2023a; Z. Abdullayev et al. 2025). However, single-band or non-simultaneous multiband observations introduce a degeneracy, as changes in the optical light curve may instead arise from intrinsic spectral evolution rather than dust destruction. Simultaneous multicolour photometry can help break this degeneracy by separating environmental effects from intrinsic emission physics (for a comprehensive optical afterglow catalogue, see M. G. Dainotti et al. 2024).

While numerous early optical observations of GRB afterglows have been conducted (e.g. C. Akerlof et al. 1999; W. T. Vestrand et al. 2005; A. Klotz et al. 2006; E. S. Rykoff et al. 2009; R. L. Becerra et al. 2021, 2023; R. Gupta et al. 2021; L. Xin et al. 2023; Y. Cheng et al. 2025), simultaneous multicolour photometry remains rare. Robotic instruments such as RAPTOR, ROTSE, TORTORA, Pi of the Sky, and MASTER-net have captured optical flashes during or immediately following the $\gamma$-ray phase (e.g. W. T. Vestrand et al. 2005; J. L. Racusin et al. 2008; E. S. Rykoff et al. 2009; E. S. Gorbovskoy et al. 2012; A. K. Ror et al. 2023a; R. Gupta et al. 2026a). These earliest optical signals are uniquely valuable because they are highly sensitive to the reverse shock propagating into the ejecta and the initial deceleration of the jet, providing crucial constraints on the jet's initial Lorentz factor and magnetization (e.g. R. Sari & T. Piran 1999). However, most detailed spectral tracking begins tens of minutes after the initial trigger (e.g. T. Krühler et al. 2011; J. Greiner et al. 2024; R. Gupta et al. 2026b).

Late-time observations provide an essential complement to rapid GRB afterglow follow-up. Once the afterglow has faded sufficiently, deep imaging can isolate the underlying galaxy and establish the position of the transient relative to the host-galaxy light distribution. Accurate astrometry, combined with the angular separation and apparent magnitude of a candidate host, enables a quantitative estimate of the probability of chance coincidence and therefore a more robust GRB–host association (e.g. J. S. Bloom, S. R. Kulkarni & S. G. Djorgovski 2002). This assessment is particularly important in crowded fields or complex environments containing neighbouring or interacting galaxies, where the nearest visible source may not necessarily be the true host. Late-time multiband imaging also provides host photometry with minimal afterglow contamination, allowing estimates of the photometric redshift, stellar mass, star-formation rate, age, and extinction when spectroscopy is unavailable. Furthermore, these observations establish the host-galaxy reference flux needed to search for an associated SN. Observations extending from the early afterglow to the host-dominated phase are therefore necessary for connecting the properties of the transient with those of its galactic environment.

Recently, T. Komesh et al. (2023a) reported the earliest known case of simultaneous *g'r'i'* observations, beginning just 58 s after the Burst Alert Telescope (BAT) trigger for GRB 201015A. This was achieved using the Nazarbayev University Transient Telescope (NUTTELA-TAO; B. Grossan, P. Kumar & G. F. Smoot 2019; Z. Maksut & B. Grossan 2021), located at the Assy-Turgen Astrophysical Observatory (Y. Aimuratov et al. 2025), which can respond to alerts and point to targets within about 8 s.

Using this capability, we present observations of the long-duration GRB 230328B. The scientific value of GRB 230328B lies in the combination of exceptionally early, strictly simultaneous multicolour photometry and extensive broad-band follow-up. NUTTELA-TAO began simultaneous $g'r'i'$ observations only 41 s after the *Swift*/BAT trigger, corresponding to approximately 16 s in the rest frame for the assumed photometric redshift of $z = 1.54$. Unlike sequential multiband measurements, these observations provide an instantaneous optical spectral slope without requiring temporal interpolation across a rapidly varying light curve. The early optical continuum remains statistically consistent with a constant spectral slope from approximately $10^2$ to $7 \times 10^3$ s. This result provides no evidence for rapid dust destruction. Furthermore, the absence of significant colour evolution across the pronounced optical rebrightening at approximately $4 \times 10^3$ s demonstrates that this feature is achromatic, favouring a dynamical origin, such as energy injection, rather than spectral evolution. Combined with the X-ray, radio, late-time optical and infrared observations, and host-galaxy characterization, these data make GRB 230328B a useful benchmark for connecting the earliest afterglow behaviour with broad-band modelling and the dusty environment of an otherwise representative long GRB.

This paper is organized as follows. Section 2 describes the prompt $\gamma$-ray, optical, X-ray, radio, and late-time host-galaxy observations, together with the corresponding data-reduction procedures. Section 3 presents the prompt-emission analysis, the

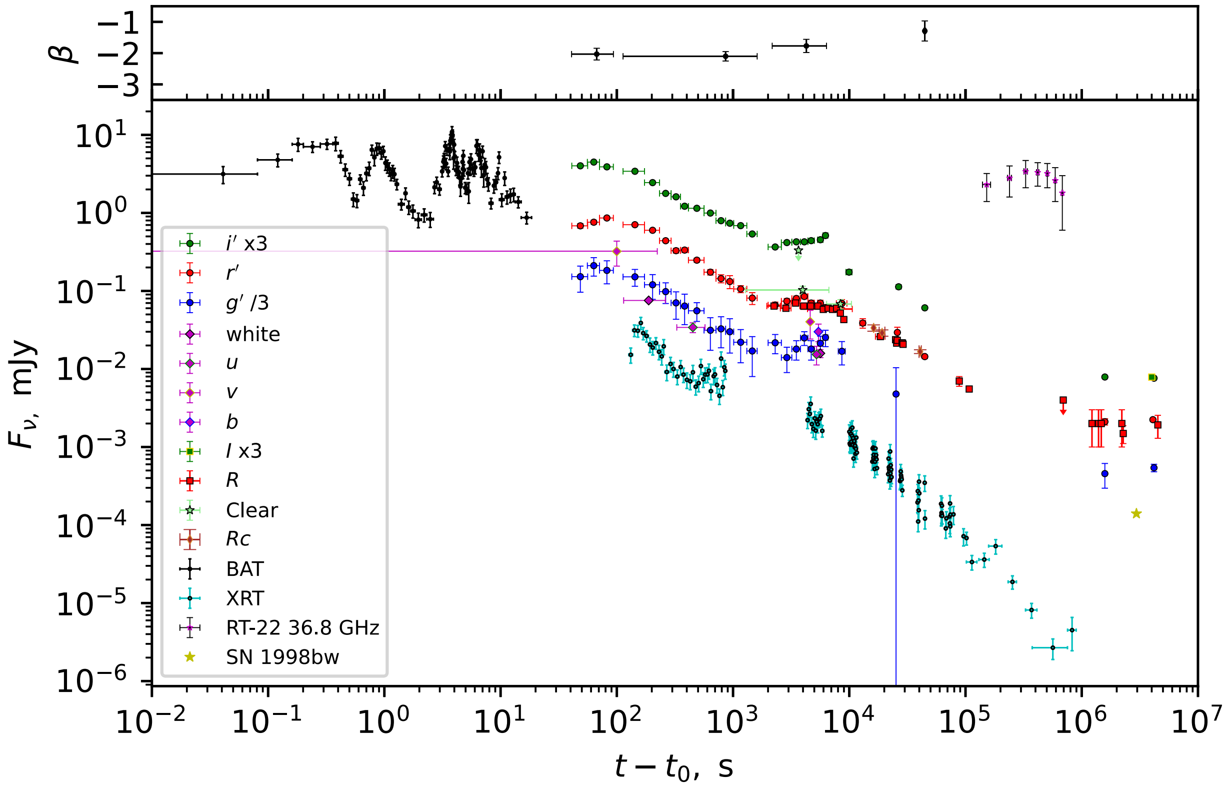


**Figure 1.** Upper panel: The observed optical spectral slope $\beta$ (without correction for a host galaxy extinction) for GRB 230328B as a function of time. We determine the spectral slope at each epoch by fitting a power law to the $g'r'i'$ fluxes and plot the time-averaged results. Bottom panel: Multiwavelength light curves including $\gamma$-ray, X-ray, optical, and radio data. Here, $t$ denotes the mid-point time of each co-add and $t_0$ is the BAT trigger time, which occurred at 14:54:48 UT on 2023 March 28 (J. D. Gropp et al. 2023). The large star denotes the flux at the maximum of a light curve of SN 1998bw-like supernova as viewed from observer frame at the distance of the GRB 230328B source $z_{\mathrm{phot}} = 1.54 \pm 0.06$. The parameters of the light curve of SN 1998bw in observer frame was calculated using multicolour SN 1998bw light curve (A. Clocchiatti et al. 2011) and proper transformation in the observer frame.

temporal and spectral properties of the afterglow, the broad-band spectral energy distribution (SED) fitting, and the physical modelling of the afterglow and its rebrightening. It also describes the identification and characterization of the host galaxy and the search for an associated SN. Finally, Section 4 summarizes the principal results and their implications.

## 2 OBSERVATIONS

We define the *early afterglow* phase as the first ~1 h after the BAT trigger; all later times are referred to as the *late afterglow*. We characterize the light-curve flux by $F_\nu \propto t^\alpha \nu^\beta$. Distinct segments or features of the light curve are labelled with numerical subscripts. All magnitudes reported throughout the paper are in the AB system and have been corrected for Galactic extinction using the extinction maps of E. F. Schlafly & D. P. Finkbeiner (2011). The full light curve is shown in Fig. 1.

### 2.1 Early afterglow observations

GRB 230328B was triggered by the Swift Burst Alert Telescope (*Swift*/BAT) at 14:54:48 UT on 2023 March 28 (J. D. Gropp et al. 2023). The same *Swift* GCN Circular reported an optical counterpart detected by the Swift Ultra-violet Optical Telescope (*Swift*/UVOT) at RA (J2000) = $19^{\mathrm{h}}24^{\mathrm{m}}01.84^{\mathrm{s}}$ and Dec. (J2000) = $+80^\circ 00' 34\farcs5$, with a 90 per cent confidence error radius of 0.62 arcsec. The BAT light curve exhibited a complex temporal structure with a duration of $T_{90} = 19.23 \pm 3.82$ s (Markwardt et al. 2023), followed by bright flaring emission detectable below 25 keV for at least 200 s after the trigger. The same Swift GCN Circular reported the time-averaged spectrum. The best fit is by a power law with an exponential cut-off with a photon index of 1.22 ±0.29, and $E_{\mathrm{peak}}$ of 99.7 ±59.7 keV. The burst was also independently detected by the *Fermi*/Gamma-ray Burst Monitor (GBM), which triggered at 14:54:47 UT, approximately 1 s before the BAT trigger. Based on $T_{90}$ duration the burst was classified as a likely long-duration GRB (Fermi GBM Team 2023).

In response to an automated GCN/BAT position alert, the NUTTELA-TAO began observations of the GRB at 14:55:29 UT on 2023 March 28, just 41 s after the BAT trigger, and continued until 6720 s post-trigger (T. Komesh et al. 2023b) simultaneously in the Sloan $g'$, $r'$, and $i'$ bands (B. Grossan et al. 2019; Z. Maksut & B. Grossan 2021). Calibration procedures involved referencing four bright, isolated, and unsaturated field stars from the Panoramic Survey Telescope & Rapid Response System (Pan-STARRS) catalogue. The data are presented in Table A1.

### 2.2 Later afterglow observations

We continued afterglow observations using telescopes from the IKI GRB-FuN network (A. Volnova et al. 2021) and several other instruments. The IKI GRB-FuN is an international collaboration coordinated by the Space Research Institute of the Russian Academy of Sciences (IKI RAS) that brings together optical telescopes distributed across different geographic longitudes to provide rapid and extended follow-up observations of GRBs. The network coordinates observations following GRB alerts to improve the temporal coverage of optical afterglows, particularly during the early and intermediate phases, and facilitates the joint analysis of data obtained with participating facilities. For GRB 230328B, observations from several IKI GRB-FuN facilities extended the temporal coverage of the optical afterglow beyond the early NUTTELA-TAO observations. The observations obtained by our collaboration and analysed in this work are described below, and the resulting photometric measurements are listed in Table A2.

The 1.5-meter telescope AZT-33IK of the Sayan Solar Observatory (Republic of Buryatia, Mondy, Russia) observed the source starting ∼30 min after the trigger and taking several frames in filter *R*. Observations continued for several epochs till 2023 April 22 (S. Belkin et al. 2023).

We observed with the Santel-400 (0.4 m) telescope of ISON-Multa observatory (Altay Republic, Russia) in the clear filter ∼1 h after the trigger and detected a fading optical afterglow (N. Pankov et al. 2023). We observed with the RC-36 telescope of the ISON-Kitab observatory (Qashqadaryo Region, Kitob, Uzbekistan) approximately at the same time with the same filter and obtained the upper limit (S. Belkin et al. 2023).

The GROWTH-India 0.7-meter telescope (GIT; H. Kumar et al. 2022) of the Indian Astronomical Observatory (Hanle, Ladakh, India) took several $g'r'i'$-band frames starting ∼1.76 h after the burst trigger. Typical observations were 300 s long and were stacked as needed. The long duration of the observations allowed us to separate all frames into seven epochs.

We also observed with the 0.7-meter AS-32 telescope of the Abastumani Astrophysical Observatory (AbAO; Abastumani-Kanobili, Georgia) in the *R* filter ∼2 h after the trigger (S. Belkin et al. 2023).

The RC500 telescope of the Ussuriysk Astrophysical Observatory (UAFO; Primorsky Krai, Ussuriysk, Russia; observatory code C15), a division of the Institute of Applied Astronomy of the Russian Academy of Science, observed the optical source at 2.3 h after the trigger in clear light, obtaining a stacked frame with a total exposure of 90×45 s and clearly detecting the source.

The 3.6-meter Devasthal Optical Telescope (DOT; S. B. Pandey et al. 2023; R. Gupta et al. 2024) of the Aryabhatta Research Institute of Observational Sciences (ARIES; Nainital, Uttarakhand, India) took several *R*-band frames starting ∼7 h after the trigger and continued observations the next night, adding one more *R*-band epoch (A. K. Ror et al. 2023b).

The late phases of the source were observed by the 6-meter Large Altazimuth Telescope (BTA) of the Special Astrophysical Observatory (SAO; Karachai-Cherkessian Republic, Nizhnij Arkhyz, Russia). We made two observational sets in April and May 2023, using $g'$, $r'$, and $i'$ filters.

We also used the 2.6-meter Shajn telescope (ZTSh) of the Crimean Astrophysical Observatory (CrAO; Crimea, Russia) to obtain deep imaging of the site in the *R*band with more than 2 h of exposure at the end of April 2023.

In May 2023, we obtained two epochs of observations with the 1.5-meter AZT-22 telescope of the Maidanak Astronomical Observatory (MAO) of the Ulugh Beg Astronomical Institute (UBAI; Qashqadaryo Viloyati, Uzbekistan) in filters *R* and *I*.

All optical data were reduced using IRAF (National Optical Astronomy Observatories & The IRAF community 2025). Standard calibration procedures, including bias subtraction, dark correction, and flat-fielding, were performed with the `ccdproc` task. To improve the signal-to-noise ratio, some images were combined using `imlintran` and `imcombine`. Aperture photometry was carried out with the APPHOT package, adopting an aperture radius equal to twice the full width at half-maximum (FWHM) of point sources measured for each night. Photometric calibration was performed using nearby comparison stars with magnitudes from the Pan-STARRS DR1 catalogue (K. C. Chambers et al. 2016; *gri* bands) and the USNO-B1.0 catalogue (D. G. Monet et al. 2003; *R* band).

In addition to our measurements, we incorporated photometry reported in GCN Circulars during the first day post-trigger: OHP/T120 ($R_c$) (C. Adami et al. 2023); GRANDMA/KNC ($R_c$); CAHA/CAFOS ($R_c$) (J. F. Agui Fernandez et al. 2023); and the Liverpool Telescope $r'$ and $i'$ (B. P. Gompertz et al. 2023). These literature data were not independently reduced in this work and are explicitly identified by their corresponding references (see also Table A2).

### 2.3 X-ray observations

The *Swift* X-Ray Telescope (*Swift*/XRT) telescope observed the X-ray afterglow starting on 2023 March 28 at 14:56:38.8 UT, i.e. ∼110.3 s since BAT trigger (J. D. Gropp et al. 2023) or ∼21 s after the peak optical emission. The observations span a duration of ∼ 900 ks following the initial trigger and predominately taken in the photon-counting (PC) mode. Although the XRT provides comprehensive temporal coverage across both the early and late afterglow phases, there are noticeable gaps in the time interval corresponding to the optical rebrightening phase ($10^3-10^4$ s after the trigger).

The X-ray data in the 0.3–10 keV band used in our analysis were obtained from the *Swift* Burst Analyser service.[1] Instead of using the 10 keV flux density provided by the service, the final X-ray light curve was derived from the 0.3–10 keV flux data and then converted to flux density using the relation: $f_X = 10^{23} F_X/\Delta\nu_{\rm XRT}$, where $F_X$ is the flux in erg cm$^{-2}$ s$^{-1}$, and $\Delta\nu_{\rm XRT}$ is the XRT bandwidth in Hz. In contrast to the flux density at a single 10 keV energy obtained after the spectral modelling, the resulting average flux density in the 0.3–10 keV band is not prone to systematic errors. The resulting X-ray light-curve afterglow behaviour is described in Section 3.2.

### 2.4 Radio observations

Observations at 36.8 GHz were conducted with the 22-m RT-22 radio telescope located at Simeiz (A. Volvach, N. Nesterov & L. Petrov 2000; A. E. Volvach, L. N. Volvach & I. D. Strepka 2012). The receiving system employed a modulation radiometer to reduce the influence of gain–instability fluctuations in the amplification chain and atmospheric brightness–temperature variations. The measurements were performed using a differential observing mode based on sequential positioning of the source within two feed horns with orthogonal polarizations. In this scheme, the recorded signal corresponds to the difference between antenna temperatures measured in alternating telescope positions

[1] https://www.swift.ac.uk/burst_analyser/01162001/

**Table 1.** Flux densities for calibration sources at 36.8 GHz.

| Source | DR 21 | 3C 274 | NGC 7027 | 3C 286 |
|---|---|---|---|---|
| Flux density (Jy) | 18.3 | 14.3 | 5.1 | 1.56 |

directed toward the source and adjacent reference regions of the sky. This strategy suppresses common-mode atmospheric and instrumental contributions.

Each observational session consisted of a sequence of 30–40 integrations. The final antenna temperature was determined from the average, while the uncertainty was estimated from the dispersion of the individual records. Independent registration in two polarization channels allowed us to derive total flux densities with reduced sensitivity to possible source polarization effects. Calibration of the antenna temperature scale was performed every 3–4 h using atmospheric elevation scans obtained over a wide range of zenith distances. Flux density was calibrated using reference radio sources with well-established characteristics listed in Table 1. The flux densities were additionally corrected for atmospheric attenuation and the elevation dependence of the effective collecting area of the telescope. The data are provided in Table A2.

### 2.5 Host galaxy observations

The source host galaxy was discovered by A. Rossi et al. (2023) ∼3 months after the burst. More than a year after the optical afterglow faded, we observed the host using the 6-meter Large Altazimuth Telescope (BTA) of the Special Astrophysical Observatory (SAO RAS), Russia. On 2024 June 14, 445 d after the burst, we obtained images in *g*, *r*, and *i* filters with exposures of 1, 1, and 0.5 h, respectively. The photometry of the host galaxy is provided in Table 5. Deep images and a seeing of 1.4 arcsec allowed us not only to detect the host galaxy, but also to resolve the structure of its neighbourhood.

We continued the observations in 2024–2025 to obtain deep multicolour images of the host to estimate the redshift modelling SED using broad-band photometry. In addition to deep *g*, *r* and *i* images from SAO/BTA, we obtained *BVRI* images using the 2.6-meter Shajn telescope of the Crimean Astrophysical Observatory (CrAO/ZTSh), infrared *J* and *K* images from the 2.5-meter telescope SAI-25 of the Caucasian Mountain Observatory (CMO/SAI-25), the *z*-band image from the 1.5-meter AZT-20 telescope of the Assy-Turgen observatory (Assy-Turgen/AZT-20) and SAI-25 telescope, and the *H*-filter image from 10-meter Gran Telescopio Canarias (GTC) equiped with **E**spectrógrafo **M**ultiobjeto **I**nfra-**R**ojo (EMIR) infrared spectrograph. Since the source is circumpolar for both the North Caucasus and Crimea, the stacked images from the ZTSh, SAI-25, and GTC telescopes were obtained during several different nights with good weather conditions and a seeing of ∼1.4–1.5 arcsec to obtain better upper limits and angular resolutions.

Near-infrared observations (*J* and *K* bands) were performed with the ASTRONIRCAM camera (A. E. Nadjip et al. 2017) mounted on the 2.5-m telescope of the Caucasian Mountain Observatory. The primary reduction procedure is described in A. M. Tatarnikov et al. (2023). The final images are sums of individual frames obtained with exposures of ∼60 s in the *J* band and ∼30 s in the *K* band, between which the telescope was moved by 3 arcsec.

All optical host galaxy observations were reduced and calibrated in the same way as described in Section 2, and IR data photometry was calibrated using the Two Micron All-Sky Survey-Point Source Catalog (2MASS-PSC). More details are given in Section 3.5.

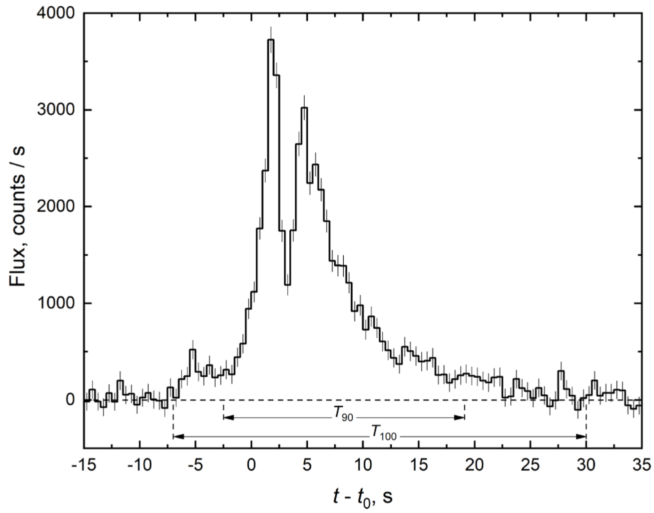


**Figure 2.** Background subtracted light curve of GRB 230328B based on the GBM/*Fermi* data from NaI_06, NaI_07, NaI_09, and BGO_01 detectors. with a time resolution of 0.5 s in the energy range of (8, 850) keV. Time intervals, covering $T_{90}$ and $T_{100}$, are shown.

### 2.6 *Fermi*/GBM prompt $\gamma$-ray observations

The GBM onboard the *Fermi* Observatory consists of 12 Na I scintillation detectors, working in the (8, 850) keV range, and two bismuth germanate (2 BGO) scintillation detectors, working in the (0.2, 40) MeV range (C. Meegan et al. 2009). The GBM/*Fermi* data used in this work were obtained from a public FTP archive.[2] GBM/*Fermi* triggered and located GRB 230328B at 14:54:47.43 UT on 2023 March 28 (S. Dalessi, C. Meegan & Fermi GBM Team 2023). We used data from NaI_06, NaI_07, NaI_09, and BGO_01 detectors in our analysis, which were the most illuminated for the source.

The background-subtracted light curve in (8, 850) keV energy range with time resolution of 0.5 s is presented in Fig. 2. We fitted the background with third-order polynomial in time ranges (−130, −20) s and (70, 470) s jointly. The light curve could not be fit by a single exponential Fast-Rise Exponential-Decay (FRED) pulse (J. P. Norris et al. 2005); it consists of several highly overlapped pulses.

The burst has a total duration of $T_{100} \simeq 37$ s, estimated using an integrated light curve with a time resolution of 0.2 s. We find that $T_{90}$ (the time interval in which the integrated counts of the GRB increase from 5 per cent to 95 per cent) is typical for a type II (long) GRB: $T_{90} = 21.6 \pm 0.4$ s. The boundaries of the $T_{100}$ and $T_{90}$ time intervals are shown in Fig. 2.

To reconstruct the photon spectrum of the burst, we used the RMFIT v4.3.2 software package, developed for analysing data from the GBM/*Fermi* experiment.[3] The technique is similar to that proposed by D. Gruber et al. (2014). The spectrum was analysed using data from the NaI_06, NaI_07, NaI_09, and BGO_01 detectors in time interval of (−7, 30) s, covering the whole burst (time interval

[2] https://heasarc.gsfc.nasa.gov/FTP/fermi/
[3] https://fermi.gsfc.nasa.gov/ssc/data/analysis/rmfit/

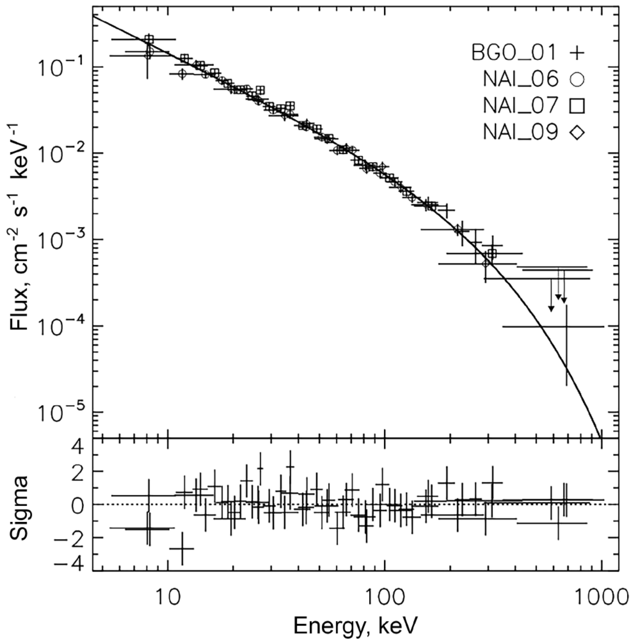


**Figure 3.** GRB 230328B photon spectrum obtained from the GBM/*Fermi* measurement in (–7, 30) s time interval with respect to the trigger time, modelled with a power law with an exponential cut-off. The top panel shows the spectrum obtained using data of the NaI_06, NaI_07, NaI_09, and BGO_01 GBM/*Fermi* detectors. The bottom panel shows the deviations between the spectral model and the experimental data expressed in units of standard deviations.

$T_{100}$). The optimal spectral model was found to be the power law with exponential cut-off (CPL) with the following parameters: $\alpha = -1.22 \pm 0.04$, $E_\mathrm{p} = 164^{+14}_{-12}$ keV. The fluence of the burst is $S = (1.02 \pm 0.04) \times 10^{-5}$ erg cm$^{-2}$ in (10, 1000) keV range. The photon spectrum of GRB 230328B is shown in Fig. 3.

The long duration ($T_{90} = 21.6$ s) and relatively soft spectrum ($E_\mathrm{p} = 164$ keV) allow the burst to be classified as type II (long) GRB (see e.g. S. Poolakkil et al. 2021).

## 3 RESULTS AND DISCUSSION

### 3.1 Prompt gamma-ray properties

As the redshift of GRB 230328B was not measured in direct spectroscopic observations, the isotropic energy release in the 1 keV–10 MeV range, $E_\mathrm{iso}$, could not be calculated. However, both the redshift and $E_\mathrm{iso}$ could be estimated using the $E_\mathrm{p,i} - E_\mathrm{iso}$ correlation (L. Amati et al. 2002). The correlation for the sample of 317 GRBs from P. Y. Minaev & A. S. Pozanenko (2020a, b, 2021) is shown in Fig. 4. The trajectory of GRB 230328B in the diagram represents the dependence on the redshift. It intersects with the $2\sigma$ correlation region of Type II bursts at $z = 0.16$, which we interpret as a lower limit of redshift. The corresponding lower limit on the total energy release in $\gamma$-rays is $E_\mathrm{iso} = 7 \times 10^{50}$ erg. The photometric redshift $z = 1.54 \pm 0.06$, estimated for the host galaxy of the burst (Section 3.5 and Table 6), is in agreement with the $E_\mathrm{p,i} - E_\mathrm{iso}$ correlation for long GRBs. For $z = 1.54 \pm 0.06$ we obtain $E_\mathrm{iso} = 6.4 \times 10^{52}$ erg.

To classify GRBs, P. Y. Minaev & A. S. Pozanenko (2020a) proposed a method, which, in addition to the $E_\mathrm{p,i} - E_\mathrm{iso}$ correlation, uses the bimodality of the GRBs duration distribution in the rest

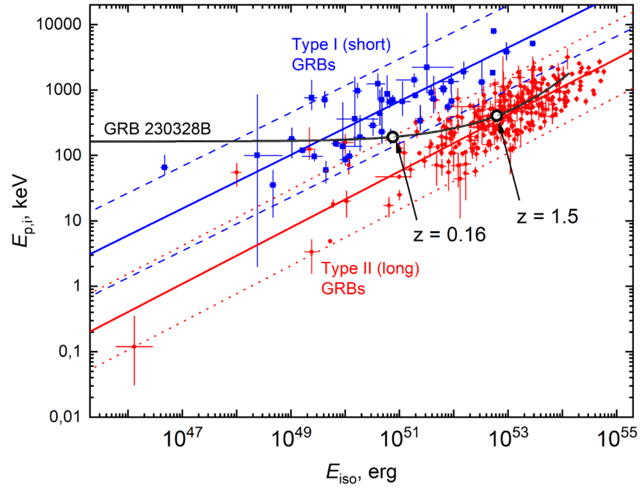


**Figure 4.** The $E_\mathrm{p,i} - E_\mathrm{iso}$ correlation for Type I (squares) and Type II (circles) GRBs with the approximate results, including $2\sigma_\mathrm{cor}$ correlation regions. The curve traces the trajectory of GRB 230328B with redshift; the position at $z = 0.16$ and $z = 1.54$ are shown by black circles.

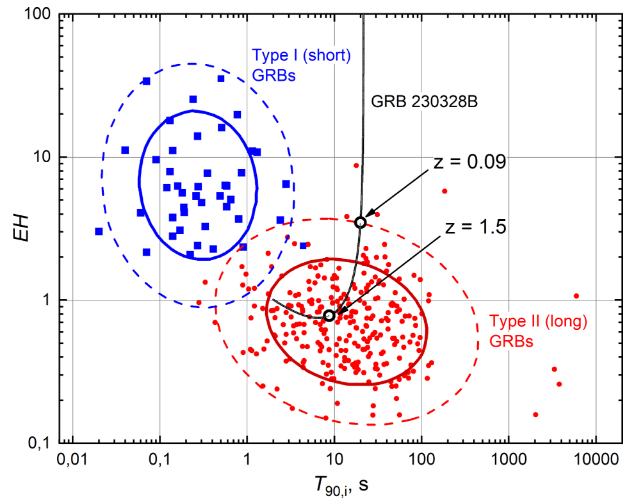


**Figure 5.** The $T_\mathrm{90,i} - EH$ diagram for Type I (squares) and Type II (circles) GRBs is shown together with the corresponding cluster analysis results, with the 68 per cent and 95 per cent confidence regions indicated by bold solid and thin dashed curves, respectively. The curve traces the trajectory of GRB 230328B with redshift, with the positions at $z = 0.09$ and $z = 1.54$ marked by black circles.

frame $T_{90,i}$. For this, the $EH$ parameter was introduced: $EH = \frac{(E_\mathrm{p,i}/100\mathrm{keV})}{(E_\mathrm{iso}/10^{51}\mathrm{erg})^{0.4}}$. It characterizes the position of a GRB on the $E_\mathrm{p,i} - E_\mathrm{iso}$ diagram: e.g. Type II GRBs are softer and brighter than Type I bursts; therefore, Type II bursts have a smaller value of the $EH$ parameter.

The $T_{90,i} - EH$ diagram is shown in Fig. 5, constructed for the GRB sample of P. Y. Minaev & A. S. Pozanenko (2020a, b, 2021). We plotted the trajectory of GRB 230328B in the diagram, varying its redshift. We estimated the lower limit, as we did before with the $E_\mathrm{p,i} - E_\mathrm{iso}$ correlation. The lower limit of redshift (intersection point of the trajectory and $2\sigma$ cluster region of Type II bursts), $z = 0.09$ is slightly less than we obtained using the $E_\mathrm{p,i} - E_\mathrm{iso}$ correlation. Again, the photometrical redshift $z = 1.54 \pm 0.06$,

**Table 2.** Parameters obtained from MCMC fitting of the optical, radio, and X-ray light curves with smoothly broken power-law models. The fit interval is the complete time range used to constrain all parameters of the corresponding component. The indices $\alpha_1$, $\alpha_3$, $\alpha_5$, and $\alpha_{1,\mathrm{X}}$ describe the pre-peak evolution, whereas $\alpha_2, \alpha_4, \alpha_6$, and $\alpha_{2,\mathrm{X}}$ describe the post-peak evolution. The parameters $t_{\mathrm{p},i}$ and $\omega_i$ denote the peak time and smoothness parameter, respectively. The optical $\chi^2$/d.o.f. refers to the joint two-component fit.

| Component | Fit interval after trigger | Parameter | Value |
|---|---|---|---|
| Optical onset | 48–1463 s | $A_1$ | $2.27 \pm 0.51$ |
| | | $\alpha_1$ | $1.25 \pm 0.41$ |
| | | $\alpha_2$ | $-1.28 \pm 0.16$ |
| | | $t_{\mathrm{p},1}$ | $89 \pm 18$ s |
| | | $\omega_1$ | $0.67 \pm 0.20$ |
| Optical rebrightening | $2.25 \times 10^3$–$1.08 \times 10^5$ s | $A_2$ | $1.00 \pm 0.03$ |
| | | $\alpha_3$ | $1.61 \pm 0.42$ |
| | | $\alpha_4$ | $-0.90 \pm 0.12$ |
| | | $t_{\mathrm{p},2}$ | $3942 \pm 256$ s |
| | | $\omega_2$ | $1.03 \pm 0.38$ |
| Optical joint fit | 48–$1.08 \times 10^5$ s | $\chi^2$/d.o.f. | 94/40 |
| Radio | $1.52 \times 10^5$–$6.81 \times 10^5$ s | $\alpha_5$ | $0.70 \pm 0.44$ |
| | | $\alpha_6$ | $-1.22 \pm 1.03$ |
| | | $t_{\mathrm{p},3}$ | $(4.21 \pm 1.28) \times 10^5$ s |
| | | $\omega_{\mathrm{radio}}$ | $2.59 \pm 1.52$ |
| | | $\chi^2$/d.o.f. | 0.28/2 |
| X-ray | $3.77 \times 10^2$–$8.26 \times 10^5$ s | $\alpha_{1,\mathrm{X}}$ | $-0.28 \pm 0.05$ |
| | | $\alpha_{2,\mathrm{X}}$ | $-1.43 \pm 0.03$ |
| | | $t_{\mathrm{p,X}}$ | $5328 \pm 432$ s |
| | | $\omega_{\mathrm{X}}$ | $1.13 \pm 0.22$ |
| | | $\chi^2$/d.o.f. | 155/118 |

measured for the host galaxy of the burst, is in good agreement with the $T_{90,i} - EH$ diagram for long GRBs.

### 3.2 Afterglow morphology

The optical and $\gamma$/X-ray light curve of GRB 230328B is shown in Fig. 1. We can identify two main features in the optical light curve: the onset bump with a peak at $\sim 10^2$ s and a rebrightening bump that peaks at $\sim 4 \times 10^3$ s. We do not observe clear signatures of a jet break.

To analyse the light curve, we use a two-component smoothly broken power law (SBPL) model, a common approach in GRB afterglow studies (e.g. E.-W. Liang, B.-B. Zhang & B. Zhang 2007; L. Li et al. 2012). The form of a single SBPL component is

$$f(t) = f_0 \left[ \left( \frac{t}{t_\mathrm{p}} \right)^{\alpha_1 w} + \left( \frac{t}{t_\mathrm{p}} \right)^{\alpha_2 w} \right]^{-1/w}, \quad (1)$$

where $f_0$ is the normalization factor, $t_\mathrm{p}$ is the peak time, $\alpha_1$ and $\alpha_2$ are the temporal indices before and after the break, and $w$ controls the sharpness of the transition. The full model is the sum of two such components

$$F(t) = f_1(t) + f_2(t), \quad (2)$$

where both $f_1$ and $f_2$ follow the form given above, but with independent parameters. To estimate the model parameters, we perform Markov chain Monte Carlo (MCMC) fitting using the PYTHON module EMCEE (D. Foreman-Mackey et al. 2013). For the optical band, due to its extensive coverage, we combine the $r'$, $R$, and $R_\mathrm{c}$ bands for fitting.

We find that $t_\mathrm{p}$ is largely insensitive to the smoothness parameter $w$, while the temporal slopes depend somewhat on $w$. Since the light curve shows smooth peaks, $w$ typically remains close to 1. The best-fitting parameters are provided in Table 2. The first optical bump was fitted over the 48–1463 s interval. The optical flux peak at $t_\mathrm{p} \sim 89 \pm 18$ s. The rise to the peak has a slope of $\alpha_1 = 1.25 \pm 0.43$, followed by a power-law decay with a slope of $\alpha_2 = -1.28 \pm 0.16$. The rebrightening component was fitted over $2.25 \times 10^3 - 1.08 \times 10^5$ s and rebrightening peaks at $3942 \pm 256$ s, with rising and declining slopes of $\alpha_3 = 1.61 \pm 0.42$ and $\alpha_4 = -0.90 \pm 0.12$, respectively.

The radio light curve was fitted over $1.52 \times 10^5$–$6.81 \times 10^5$ s. Radio emission peaks at $t_{\mathrm{p},3} = (4.21 \pm 1.28) \times 10^5$ s, with rising and declining slopes of $\alpha_5 = 0.70 \pm 0.44$ and $\alpha_6 = -1.22 \pm 1.03$, respectively.

The X-ray light curve was fitted over $3.77 \times 10^2$–$8.26 \times 10^5$ s. The late-time declining slope of the X-ray light curve after the rebrightening is $\alpha_{2,\mathrm{X}} = -1.43 \pm 0.03$, which is somewhat steeper than the contemporaneous optical slope of $\alpha_4 = -0.90 \pm 0.12$. The shallower optical slope could be a result of the sparse optical coverage beyond a few $10^4$ s; therefore, we refrain from drawing firm conclusions from this difference.

### 3.3 Afterglow broad-band spectra

To construct the broad-band spectra, we combined the $g'r'i'$ -photometry of NUTTELA-TAO, and *Swift*/XRT 0.3–10 keV spectral data in a time window $10^3$–$10^4$ s after the GRB trigger. We used HEASOFT v6.29 utilities [FTOOLS;[4] J. K. Blackburn 1995; J. K. Blackburn et al. 1999; Nasa High Energy Astrophysics Science Archive Research Center (Heasarc) 2014]. The photometric measurements in the $g'r'i'$ filters were converted to Pulse Height Amplitude (PHA) files using `flx2pha` utility. To obtain the XRT

[4] https://heasarc.gsfc.nasa.gov/ftools

**Table 3.** Results of the multiwavelength fittings to the afterglow SED obtained in the time window of $10^3$–$10^4$ s after the GRB trigger. The values of $E_{B-V}$, $R_V$, $A_V$, and $N_{\rm H}$ for the Galaxy were fixed: $E_{B-V} = 0.069$ mag, $R_V = 3.08$, and $N_{\rm H} = 0.0507 \times 10^{22}$ cm$^{-2}$.

| Ext. law | $E_{B-V}$ mag | $N_{\rm H}$ $10^{22}$ cm$^{-2}$ | $\beta$ | $\chi^2/d.f.$ |
|---|---|---|---|---|
| MW | $0.26 \pm 0.02$ | $0.22 \pm 0.16$ | $-0.80 \pm 0.02$ | 14.7/12 |
| LMC | $0.22 \pm 0.02$ | $0.18 \pm 0.16$ | $-0.78 \pm 0.02$ | 36/12 |
| SMC | $0.18 \pm 0.02$ | $0.11 \pm 0.16$ | $-0.73 \pm 0.02$ | 60/12 |

spectra, we used the *Swift* Burst Analyser service. We grouped initial spectral channels by 25 to increase the signal-to-noise ratio of individual measurements using grppha tool. The SEDs were fitted using the absorbed power law model according to P. Schady et al. (2010), which accounts for UV/optical/IR attenuation by dust particles and photoelectric absorption of X-ray radiation.

We find that a broken power-law model provides a poor fit to the observed SED; therefore, the broken power-law fitting results are not provided in the paper. The absorbed spectral model as implemented in XSPEC is given by

$$\texttt{zdust} \times \texttt{zdust} \times \texttt{phabs} \times \texttt{zphabs} \times \texttt{powerlaw}, \quad (3)$$

where zdust are UV/opt/IR extinction curves (Y. C. Pei 1992) separately for the Galaxy and the host galaxy. phabs and zphabs are photoelectric absorption of X-rays in the Galaxy and in the host galaxy, in turn. powerlaw component is a power law model in the energy domain $F_E \propto E^{-\Gamma}$, where $\Gamma$ is a photon index. We fixed Galactic parameters to $E_{B-V} = 0.069$ (E. F. Schlafly & D. P. Finkbeiner 2011) and $N_{\rm H} = 0.0507 \times 10^{22}$ cm$^{-2}$, calculated using built-in absorption maps in XSPEC. The redshift for the Galactic component zdust was fixed at $z = 0$, while for the host zdust the redshift was set at $z = 1.54$, as estimated in Section 3.5. The ISM element abundance wilm (J. Wilms, A. Allen & R. McCray 2000) was chosen instead of the solar one. We tested three different host galaxy extinction curves: the Milky Way (MW), the Large Magellanic Cloud (LMC), and the Small Magellanic Cloud (SMC). The fit was performed with the Levenberg–Marquardt method. The results of our multiwavelength SED fitting are summarized in Table 3.

Among the tested extinction laws, the MW and LMC curves provide better fits to the data, with lower reduced chi-square values compared to the SMC law. This suggests that the host galaxy dust properties in the line-of-sight may better resemble MW or LMC dust distributions rather than the steeper UV extinction characteristic of the SMC. The MW extinction $A_V = 0.80 \pm 0.06$ mag, the reddening $E_{B-V} = 0.26 \pm 0.02$, and the hydrogen column density $N_{\rm H} = (0.22 \pm 0.16) \times 10^{22}$ cm$^{-2}$ are in good agreement with the values obtained from host galaxy analysis (Section 3.5). Additionally, we compared the estimated absorption parameters with those listed in the sample of GRB hosts presented in S. Covino et al. (2013). Fig. 6 illustrates the position of the GRB 230328B host on the $N_{\rm H} - A_V$ correlation for the best-fitting parameters.

This indicates that the host of GRB 230328B is highly absorbed. Such properties are consistent with a spiral galaxy, as proposed in Section 3.5, with characteristics similar to the LMC or the MW. At $z \sim 1.54$, the inferred absorption may place the burst in an active star-forming region. Alternatively, the high absorption could arise if the GRB is located on the far side of the host disc, resulting in a large optical depth along the line of sight.

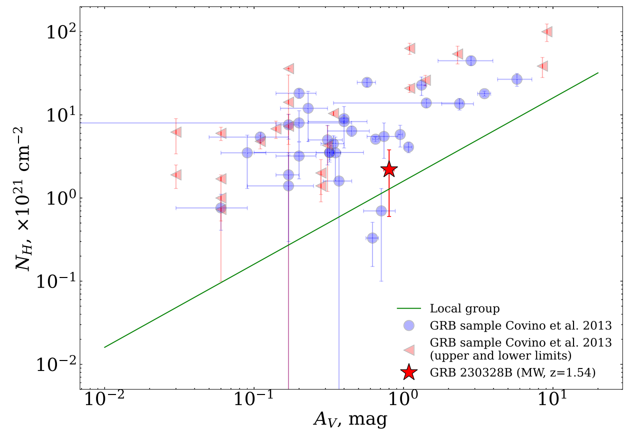


**Figure 6.** The dust-to-gas ratio of GRB 230328B host (star; obtained for the MW extinction law) in comparison with the sample of the GRB hosts from S. Covino et al. (2013). Dots are values and triangles are upper or lower limits. The line indicates the dust-to-gas ratio for the Local group of galaxies for which $N_{\rm H}/A_V \sim 1.6 \times 10^{21}$ cm$^{-2}$ mag$^{-1}$.

### 3.4 Afterglow modelling

We perform an MCMC fit to the afterglow data using the numerical code of R. Gill & J. Granot (2018, 2023). To model the optical extinction, we use the public PYTHON library DUST_EXTINCTION (K. D. Gordon 2024) with the MW extinction law (Section 3.3).

As noted above, the GRB 230328B afterglow exhibits a rebrightening bump. Such bumps are commonly observed in GRBs (e.g. E.-W. Liang et al. 2013; X.-G. Wang et al. 2015; E. Mazaeva, A. Pozanenko & P. Minaev 2018; D. Akl et al. 2026; C. Angulo-Valdez et al. 2026; S.-Y. Fu et al. 2026), and several mechanisms have been proposed to explain them (M. V. Barkov & A. S. Pozanenko 2011; B. Zhang, X.-Y. Wang & J.-H. Zheng 2024). These include two-component jets, where the onset bump originates from the jet core and the rebrightening from a wider jet wing (e.g. F. Peng, A. Königl & J. Granot 2005; O. Mukazhanov, E. Abdikamalov & P. Beniamini 2026); late energy injection (R. Sari & P. Mészáros 2000; B. Zhang & P. Mészáros 2002; T. Laskar et al. 2015; C. Angulo-Valdez et al. 2026; S.-Y. Fu et al. 2026); long-lived reverse shocks (Z. L. Uhm et al. 2012); structured jets (e.g. E. Berger et al. 2003; L.-W. Jia et al. 2012); and off-axis viewing geometries (e.g. E. Abdikamalov & P. Beniamini 2025).

Here, we explore the energy injection model recently used by C. Angulo-Valdez et al. (2026). This model considers a spherical blast wave with initial isotropic-equivalent kinetic energy $E_{\rm k,iso}$ and coasting bulk Lorentz factor $\Gamma_0$. Additional energy, $E_{\rm inj} = f_{\rm inj} E_{\rm k,iso}$, is injected into the expanding blast wave starting at radius $R_0$ and ending at $(1 + \Delta R/R_0)R_0$. This energy is added gradually as a power law,

$$\frac{{\rm d}E}{{\rm d}R} = \frac{(1+\ell)}{\Delta R} E_{\rm inj} \left( \frac{R - R_0}{\Delta R} \right)^{\ell} \propto R^{\ell} \,,$$

where $\ell$ is a parameter that characterizes the energy injection rate. Thus, the total blast wave energy grows as $E(R) \propto R^{1+\ell}$.

The MCMC fit result is given in Table 4. The light curve is shown in Fig. 7 and the corner plot is in Fig. A1. The model describes the X-ray and optical emission well, but it is less successful in reproducing the radio signal. The peak in the modelled radio light curve is caused by the passage of the injection (characteristic) frequency $\nu_m$, and occurs slightly earlier than the observed peak. Since the afterglow model is agnostic to how energy is in-

**Table 4.** Parameters for GRB 230328B obtained from the afterglow MCMC fit using an energy injection model, quoted as posterior medians with $1\sigma$ uncertainties. $E_{\rm k,iso}$ and $\Gamma_0$ denote the isotropic-equivalent kinetic energy and initial jet Lorentz factor. $p$ is the electron power-law index, while $\varepsilon_e$ and $\varepsilon_B$ are the electron and magnetic-field energy fractions. The circumburst medium is described by density $n_0$ and profile index $k$, and energy injection by $f_{\rm inj}$ and $\ell$. Finally, $R_0$ and $\Delta R/R_0$ specify the initial radius and relative shell thickness.

| Parameter | Value | Parameter | Value |
|---|---|---|---|
| $\log_{10} E_{\rm k,iso}$ | $53.92^{+0.20}_{-0.18}$ | $k$ | $0.39^{+0.16}_{-0.17}$ |
| $\log_{10} \Gamma_0$ | $3.50^{+0.28}_{-0.34}$ | $A_V$ | $0.48^{+0.05}_{-0.05}$ |
| $\log_{10} n_0$ | $-1.02^{+0.78}_{-0.84}$ | $f_{\rm inj}$ | $3.29^{+0.61}_{-0.56}$ |
| $p$ | $2.39^{+0.03}_{-0.03}$ | $\ell$ | $0.02^{+0.02}_{-0.01}$ |
| $\log_{10} \varepsilon_e$ | $-1.91^{+0.18}_{-0.19}$ | $\log_{10} R_0$ | $17.70^{+0.27}_{-0.25}$ |
| $\log_{10} \varepsilon_B$ | $-3.70^{+0.61}_{-0.57}$ | $\Delta R/R_0$ | $1.73^{+0.31}_{-0.30}$ |

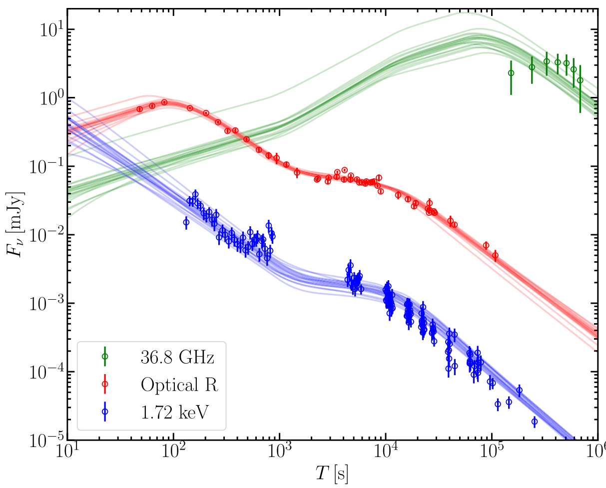


**Figure 7.** The light curves obtained from MCMC analysis together with observed data points in the radio, optical $R$, and X-ray bands, shown with dots. See Table 4 for the values of the best-fitting parameters.

jected into the blast wave, it is possible that the shock microphysical parameters, which are kept fixed, might change during this process, delaying the peak to later times. Alternatively, the radio emission might be coming from a separate emission component, e.g. the reverse shock that may arise due to the refreshing of the shock by slower-moving shells behind the outer decelerating shell.

Our MCMC fit converges on a solution where the initial blast wave is highly relativistic ($\Gamma_0 \approx 3160$) and energetic ($E_{\rm k,iso} \approx 8.3 \times 10^{53}$ erg). It propagates through an external medium with a shallow density profile ($n \propto R^{-k}$) where $k \approx 0.39$ and a density normalization $n_0 \approx 0.10$ at a radius of $10^{18}$ cm. Such intermediate density profiles ($0 < k < 2$), departing from canonical homogeneous ISM ($k = 0$) or pure wind ($k = 2$) environments, are frequently reported in afterglow modelling (e.g. X. Tian et al. 2022), but the physics behind it is not entirely clear. The dynamical parameters of the blast wave and the properties of the external medium dictate the radius at which the blast wave decelerates after sweeping up mass $M_{\rm sw} = M_0/\Gamma_0 = E_{\rm k,iso}/\Gamma_0^2 c^2$ in the thin-shell approximation (R. Sari & T. Piran 1995), where $M_0$ is the baryon load of the ejecta. The corresponding observer-frame time for the deceleration is $T_{\rm dec} = (1 + z)[(3-k)E_{\rm k,iso}/(2^{5-k}\pi A c^{5-k}\Gamma_0^{2(4-k)})]^{1/(3-k)} \simeq 0.13$ s when using the best-fitting parameters from our model. This time-scale is much shorter than the duration of the prompt emission that has a $T_{90} = 21.6$ s. The thin-shell approximation demands that $T_{\rm dec} > T_{90}$, which is achieved when $\Gamma_0 \lesssim 500$, which is more typical, while keeping all other model parameters fixed. Therefore, the large $\Gamma_0$ obtained in the fit should be treated as an upper limit rather than a true value, where the latter remains uncertain due to the missing peak of the X-ray light curve that is generally used to constrain $T_{\rm dec}$. For $T > T_{\rm dec}$ the dynamical evolution of the blast wave becomes self-similar and therefore independent of $\Gamma_0$.

When comparing the prompt isotropic-equivalent $\gamma$-ray energy ($E_{\gamma,\rm iso} = 6.4 \times 10^{52}$ erg) to the initial kinetic energy, we estimate a prompt radiative efficiency of $\eta_\gamma \equiv E_{\gamma,\rm iso}/(E_{\gamma,\rm iso} + E_{\rm k,iso}) \approx 7$ per cent. This value is consistent with expectations for internal energy dissipation mechanisms in GRB jets (Y. Fan & T. Piran 2006; P. Beniamini, L. Nava & T. Piran 2016). The true kinetic energy of the bipolar jets depends on the beaming correction that yields $E_{\rm k} = (1 - \cos\theta_j)E_{\rm k,iso} \simeq \theta_j^2 E_{\rm k,iso}/2 \simeq 4.1 \times 10^{51}\theta_{j,-1}^2$ erg, which is standard when assuming a typical jet opening angle of $\theta_j = 0.1\theta_{j,-1}$ rad. When the $1/\Gamma$ angular size of the beaming cone of radiation around the observer's line of sight, for which we assume $\theta_{\rm obs} = 0$, grows beyond $\theta_j$ as the blast wave slows down, the afterglow light curve shows an achromatic steepening, commonly referred to as a *jet break*, due to missing emission from outside of the jet core. The jet break time for the assumed jet structure and viewing geometry is given by $T_j = (\Gamma_0\theta_j)^{2(4-k)/(3-k)} T_{\rm dec} \simeq 12.5$ d, however, the late-time afterglow observations are insufficient to confirm the presence of a jet break.

The microphysics parameters describe a weakly magnetized forward shock ($\varepsilon_B \approx 2.0 \times 10^{-4}$, $\varepsilon_e \approx 0.012$), which fall within the typical ranges inferred from broad afterglow sample studies (e.g. S.-X. Yi, X.-F. Wu & Z.-G. Dai 2013; X.-G. Wang et al. 2015) The inferred electron power-law index ($p = 2.39 \pm 0.03$) is tightly constrained and aligns well with the canonical values (E.-W. Liang et al. 2013; L. Li et al. 2018). The host extinction parameter is found to be $A_V = 0.48^{+0.05}_{-0.05}$.

The rebrightening is driven by the energy injection process, characterized by an injection factor $f_{\rm inj} \approx 3.29$ and temporal index $\ell \approx 0.02$. Energy injection commences at $R_0 \approx 5.0 \times 10^{17}$ cm and continues over a fractional radial width of $\Delta R/R_0 \approx 1.73$. The amount of injected energy is significant, but not unprecedented and has been required at a similar or higher levels to explain such rebrightenings in other GRBs (e.g. T. Laskar et al. 2018; G. Schroeder et al. 2024, 2025; S. Wet et al. 2024; C. Angulo-Valdez et al. 2026). As a result, the total kinetic energy budget of the blast wave now becomes $E_{\rm k} = (1 + f_{\rm inj})E_{\rm k,0} \simeq 1.8 \times 10^{52}\theta_{j,-1}^2$ erg, where $E_{\rm k,0}$ is the kinetic energy of the initial blast wave before energy injection. The total energy budget is at the high end of the distribution but remains consistent with earlier estimates. For example, J. S. Bloom, D. A. Frail & S. R. Kulkarni (2003) find a mean beaming corrected prompt $\gamma$-ray energy for a sample of 29 GRBs to be $\langle E_\gamma \rangle \simeq 1.33 \times 10^{51}$ erg, and when assuming a typical $\gamma$-ray efficiency of $\eta_\gamma = 0.1$, the mean kinetic energy is $\langle E_{\rm k} \rangle \simeq 1.2 \times 10^{52}$ erg. The energy of the blast wave gradually grows over radius after injection and correspondingly over observer-frame time, such that $E_{\rm k}(T) \propto T^{(1+\ell)/[3-(\ell+k)]}$ (see e.g. R. Gill et al. 2026 for scalings). We can compare our parametrized energy-injection model to a particular scenario, e.g. when the inner ejecta that energizes the outer (initial) ejecta has a radial velocity stratification, i.e. $M(\Gamma) \propto \Gamma^{-s}$, so that

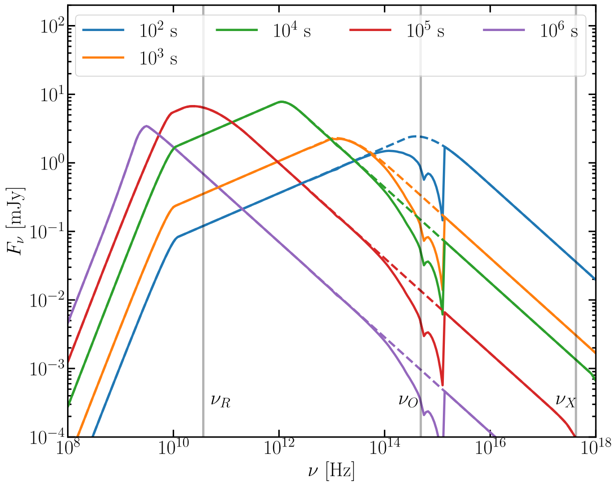


**Figure 8.** Afterglow spectra corresponding to best-fitting parameters obtained from MCMC analysis at various epochs. The solid lines include the extinction of the host, while dashed lines do not. The vertical grey lines indicate the frequencies at which observations were obtained.

more mass and kinetic energy resides in the slower moving ejecta (R. Sari & P. Mészáros 2000). In this scenario, the blast wave energy grows as $E_\mathrm{k}(T) \propto T^{-(3-k)(1-s)/(7+s-2k)}$ that yields $s = (4 - k + \ell)/(2 - k - \ell) = 2.3$ when comparing it with our model.

Spectra from this model are shown in Fig. 8 at various epochs. The radio emission remains above the self-absorption frequency ($\nu_a$) at all times. The optical emission lies in the slow-cooling regime, $\nu_\mathrm{m} < \nu_O < \nu_\mathrm{c}$, at all times. The cooling frequency $\nu_\mathrm{c}$ starts entering the X-ray band at $\simeq 10^5$ s. The spectrum is consistent with the finding from the SED fit (Section 3.3) that it can be fitted with a single optical–X-ray power law over $10^3$–$10^4$ s.

To further support this, the observed optical spectral slope ($\beta$; Fig. 1, upper panel) from simultaneous $g'r'i'$ NUTTELA-TAO photometry yields an inverse-variance weighted mean of $\bar{\beta} = -2.00 \pm 0.10$ across three intervals ($\beta_{41\text{-}93\mathrm{s}} = -2.03 \pm 0.18$, $\beta_{113\text{-}1613\mathrm{s}} = -2.10 \pm 0.15$, $\beta_{2004\text{-}6900\mathrm{s}} = -1.78 \pm 0.21$). A constant-slope fit ($\chi^2 = 1.57$, 2 d.o.f., $p = 0.46$) indicates no significant colour evolution over $\simeq 10^2$–$7 \times 10^3$ s. Later Liverpool $r'i'$ observations at $4.46 \times 10^4$ s are modestly bluer ($\beta = -1.29 \pm 0.32$, a $\sim 2\sigma$ difference), but are limited to two bands. We therefore adopt a nearly constant optical continuum, supporting our model finding that the intrinsic afterglow optical emission remains in the slow-cooling regime for most of its evolution.

While our data are consistent with the energy injection interpretation, several caveats apply. Most importantly, we fit a 12-parameter model, and the high dimensionality makes it difficult to fully exclude local minima. Furthermore, the early X-ray data exhibit flaring, and the lack of contemporaneous radio coverage limits the constraints on parameters shaping the early afterglow. Finally, while energy injection naturally explains the rebrightening, we cannot completely rule out alternative physical scenarios, such as a structured two-component jet (O. Mukazhanov et al. 2026).

### 3.5 Host galaxy

Fig.9 shows the stacked image of the *gri* filters taken 445 d after the burst trigger. The localization of the source is marked by a cross. The nearest visual environment of the source position is complex, revealing the conglomerate of possibly several interacting galaxies. To avoid contamination, we studied only the brightest part of the structure, marked in Fig. 9 as Gh, assuming that this is the host galaxy of GRB 230328B. Assuming the coordinates of the optical afterglow from J. D. Gropp et al. (2023) with the uncertainty of 0.62 arcsec and taking the galaxy brightness from CrAO/ZTSh filter $R = 24.03 \pm 0.08$ we estimate the probability of chance association between the host galaxy and the optical transient using equations (1–3) from J. S. Bloom et al. (2002) as $P_\mathrm{ch} = 0.52$ per cent. Thus we can conclude that the source Gh is the host galaxy of the GRB 230328B.

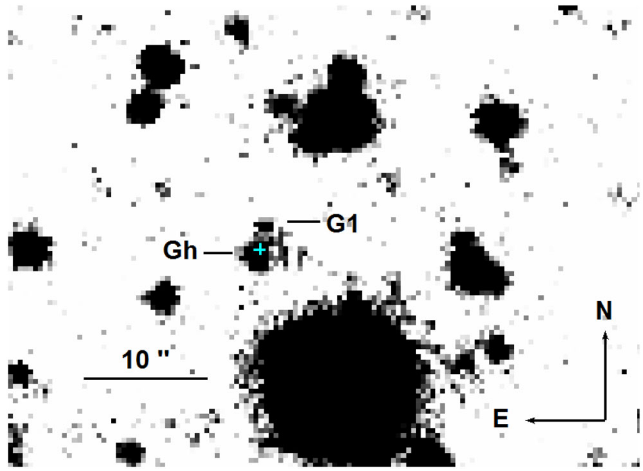


**Figure 9.** The localization region of the GRB 230328B observed by the 6-m BTA telescope of SAO RAS 445 d after the burst trigger, *gri* combined image. The cross indicates the position of the GRB optical afterglow detected by *Swift*/UVOT at RA (J2000) = $19^\mathrm{h}24^\mathrm{m}01.84^\mathrm{s}$, Dec. (J2000) = $+80^\circ00'34''.5$ with an uncertainty of 0.62 arcsec (J. D. Gropp et al. 2023). The host galaxy is marked as Gh. A possible interacting neighbour galaxy is marked as G1.

The host galaxy Gh is clearly detected with the neighbouring structure in all bands except $B$, $V$, and $H$. The photometry of the host was made using APPHOT task of the NOAO's IRAF software package.[5] To minimize the contribution of neighbouring sources and to collect equivalent flux for every filter, we chose a fixed circular aperture with the diameter of 3.5 arcsec centred on the brightness centre of the Gh source from the stacked BTA $g'r'i'$ image, i.e. at RA (J2000) = $19^\mathrm{h}24^\mathrm{m}02.03^\mathrm{s}$, Dec. (J2000) = $+80^\circ00'33''.9$ (with statistical error of 0.5 arcsec). The offset of the afterglow position (J. D. Gropp et al. 2023) from the host galaxy centre lies within the statistical errors of the measurements of 0.8 arcsec. Hence, we can place only the upper limit of the offset of 7 kpc. The photometry of the host galaxy is listed in Table 5. All magnitudes were corrected for the Galactic reddening using maps of extinction from E. F. Schlafly & D. P. Finkbeiner (2011).

We used the LE PHARE software package (S. Arnouts et al. 1999; O. Ilbert et al. 2006) to model the broad-band photometry of the host with a synthetic SED. We used the PEGASE2 library of population synthesis models (M. Fioc & B. Rocca-Volmerange 1997) to obtain the best-fitting SED and the main physical parameters of the galaxy: its type, redshift, average bulk extinction,

[5] https://iraf-community.github.io/x11iraf.html

**Table 5.** Photometry of the host galaxy. In the first three columns filter name, effective average wavelength, and effective FWHM are listed. $A_{\rm MW}$ shows the value of the Galactic extinction subtracted from the magnitude of the host galaxy for every filter, based on the extinction maps from E. F. Schlafly & D. P. Finkbeiner (2011). $T_{\rm exp}$ is the exposure time. UL gives the $3\sigma$ upper limit sensitivity in magnitudes for images of the given exposure time.

| Filter | $\lambda_{\rm eff}$, Å | $\Delta\lambda$, Å | $A_{\rm MW}$ | $T_{\rm exp}$ (s) | mag (err) | UL | Obs./Tel. |
|---|---|---|---|---|---|---|---|
| *B* | 4370 | 820 | 0.247 | 27 120 | – | 24.0 | CrAO/ZTSh |
| *g* | 4920 | 710 | 0.225 | 3600 | 24.33 (0.06) | 26.0 | SAO/BTA |
| *V* | 5420 | 890 | 0.183 | 13 560 | – | 24.0 | CrAO/ZTSh |
| *r* | 6540 | 900 | 0.156 | 3600 | 23.89 (0.07) | 26.1 | SAO/BTA |
| *R* | 6600 | 1570 | 0.148 | 14 640 | 24.03 (0.08) | 25.4 | CrAO/ZTSh |
| *i* | 7540 | 1300 | 0.116 | 1800 | 23.48 (0.09) | 25.1 | SAO/BTA |
| *I* | 7600 | 1210 | 0.103 | 5520 | 23.71 (0.15) | 24.0 | CrAO/ZTSh |
| *z* | 8960 | 990 | 0.086 | 2700 | 23.31 (0.16) | 23.9 | CMO/SAI-25 |
| *J* | 12 410 | 2150 | 0.048 | 7200 | 22.46 (0.17) | 23.2 | CMO/SAI-25 |
| *H* | 16 290 | 2810 | 0.031 | 16 200 | – | 21.8 | EMIR/GTC |
| *K* | 21 660 | 2780 | 0.021 | 7200 | 22.31 (0.27) | 22.4 | CMO/SAI-25 |

**Table 6.** Physical parameters of the host galaxy Gh.

| | | | |
|---|---|---|---|
| Redshift | $z$ | = | $1.54 \pm 0.06$ |
| Type | S0 | | |
| Diameter | $d$ | ∼ | 28 kpc |
| Abs. *R* magnitude[a] | $M_R$ | = | –22.0 |
| Bulk extinction[b] | $E_{B-V}$ | ∼ | 0.2 |
| Age | $t$ | = | $7.1 \times 10^8$ yr |
| Mass | $M$ | = | $1.6 \times 10^{10}$ $M_\odot$ |
| Star form. rate | SFR | = | 35 $M_\odot$ yr$^{-1}$ |

[a] *R* filter in the observer frame.
[b] Assuming the Milky Way extinction law from M. J. Seaton (1979).

age, mass, and star formation rate. According to the results, the host galaxy is a relatively young S0-type galaxy with a redshift of $z = 1.54 \pm 0.06$ with a size similar to the Milky Way: assuming the angular size of the photometry aperture of 3.5 arcsec as the host angular size, we estimate its physical dimension as $\sim 28$ kpc.[6] All host parameters are listed in Table 6. Fig. 10 shows the best-fitting host SED along with the corresponding photometry of the galaxy and the probability density function for the best model ($\chi^2/DOF = 4.4/8$).

Deep SAO RAS/BTA imaging of the host galaxy region (Fig. 9) reveals a much fainter component G1 (the estimated flux is $\sim 25$ per cent of that of Gh, i.e. 1.5 mag fainter than Gh based on the BTA *gri*-sum aperture instrumental photometry of the two objects) located north-west of Gh. If indeed this source G1 is a neighbouring galaxy at an angular distance of about 2.5 arcsec between the centres of the galaxies, then the system could be an interacting pair of galaxies at a distance of ∼20 kpc at $z = 1.54$. Some long GRB hosts show ongoing star formation, and interacting systems are not unprecedented: several GRBs have been found in galaxies exhibiting clear signs of interaction or merging (see e.g. A. A. Volnova et al. 2014; M. Jelínek et al. 2025).

Fig.11 shows the position of the host galaxy of GRB 230328B in the stellar mass–star formation rate plane, compared to a compiled sample of long GRBs, short GRBs, long GRBs with associated SNe, and long GRBs without detected SNe (e.g. S. Savaglio, K. Glazebrook & D. Le Borgne 2006, 2009; K. Taggart & D. A. Perley 2021; R. Gupta et al. 2022; A. E. Nugent et al. 2022). With $\log(M_\star/{\rm M}_\odot) \approx 10.2$ and ${\rm SFR} \approx 35\,{\rm M}_\odot\,{\rm yr}^{-1}$, the host of

[6]For distances calculations, we used the NED Cosmology Calculator by E. L. Wright (2006) with $H_0 = 69.6$ km s$^{-1}$ Mpc$^{-1}$, $\Omega_M = 0.286$, and $\Omega_\Lambda = 0.714$.

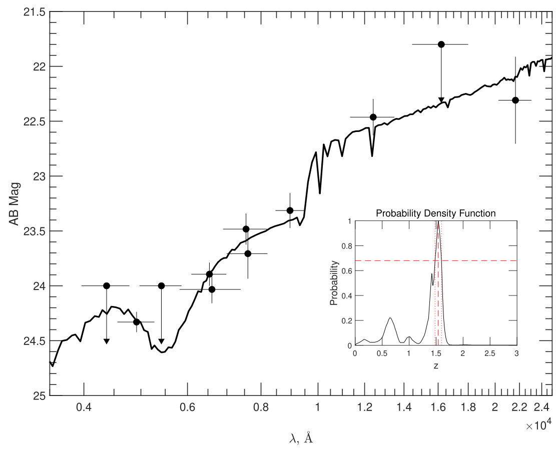


**Figure 10.** The host galaxy spectral energy distribution modelled with the broad-band photometry for the redshift estimation. Circles depict the extragalactic magnitudes of the host in the filters *BgVrRIizJHK*. *Y*-axis error-bars are $1\sigma$ photometric errors, X-error-bars are filter weights magnitudes determined as FWHM/2 of the bandwidth of the filter. Arrows mark upper limits. Solid line is the best modelled host SED from the PEGASE2 library for the S0-type galaxy at the redshift $z = 1.54 \pm 0.06$ with $E_{B-V} \sim 0.2$. The inset displays the probability density function (solid line) of the model of the redshift, the horizontal dashed line depicts $1\sigma$ (68 per cent) level, the vertical dashed line marks the maximum probability redshift for the model, and the two dotted lines mark $1\sigma$ boundaries of the best-modelled redshift.

GRB 230328B occupies the high-mass, actively star-forming end of the long GRB host distribution, lying above the star-forming main sequence (dashed line; D. Elbaz et al. 2011). These properties are characteristic of massive, collapsar-type GRB hosts (T. Krühler et al. 2015).

### 3.6 Searching for supernova

It is well known that some long-duration GRBs are accompanied by Type Ic SNe (e.g. Y.-D. Hu et al. 2021; Y. Aimuratov et al. 2023; G. Finneran et al. 2025). However, SN searches are generally effective only at low redshift, as at higher redshifts the sensitivity of current instruments is often insufficient to detect an SN against the host galaxy background (R. Gupta et al. 2025).

The redshift of GRB 230328B was not determined during the afterglow phase. Nevertheless, we conducted a search for an SN signature, as each additional detection provides valuable constraints

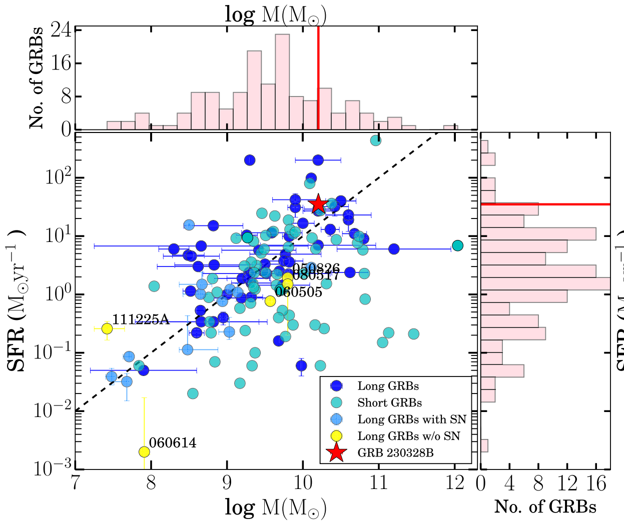


**Figure 11.** Stellar mass versus star formation rate (SFR) for the host galaxy of GRB 230328B (star) compared to a compiled sample of GRB host galaxies, including long GRBs, short GRBs, long GRBs with associated supernovae (circles with cross-hatching), and long GRBs without detected supernovae (GRBs 050826, 060505, 060614, 080517, and 111225A). The dashed line represents the star-forming main sequence. Marginal histograms show the distributions of stellar mass (top) and SFR (right) for the full comparison sample; the vertical and horizontal lines mark the values derived for GRB 230328B. The host galaxy of GRB 230328B occupies the high-mass, very high-SFR end of the distribution.

on the population of GRB-associated SNe. We monitored the GRB localization region from 3 to 48 d after the trigger (Table A2).

No statistically significant excess in the source brightness (i.e. host galaxy plus a potential SN) was detected in any of the filters ($g'$, $R$, $r'$, $i'$) over this period. The photometry remained consistent across epochs, allowing us to place upper limits on any SN contribution. Using the deepest observations, we constrained the maximum brightness a SN could have had without being detected. We utilized BTA/SAO RAS observations obtained at 18 and 48 d post-trigger. The positive $3\sigma$ photometric uncertainties at these epochs provide upper limits on the total flux from the host galaxy and any SN component. From these data, we derive limiting magnitudes of $i' = 23.2$ at 18.3 d and $i' = 23.1$ at 48.4 d. At the redshift of $z = 1.54$, these values correspond to absolute magnitudes of $-22.0$ in the $u'$ filter at 7.3 and 19.4 d in the GRB rest frame. (These magnitudes are not corrected for the host galaxy extinction.)

A natural question is whether GRB 230328B could belong to the rare class of long-duration GRBs lacking an associated SN. The confirmed SN-less long-duration GRBs, most notably GRB 060614 (J. P. U. Fynbo et al. 2006; N. Gehrels et al. 2006) – form a clearly distinct sub-population in Fig. 11, residing exclusively in low-mass ($\log(M_\star/\mathrm{M}_\odot) \lesssim 10$), low-SFR dwarf galaxies, separated from the host of GRB 230328B by a few orders of magnitude in both stellar mass and SFR. The host of GRB 230328B bears no resemblance to this class in any of its global properties, strongly disfavouring an SN-less long GRB classification based on host galaxy evidence alone.

We note that at $z = 1.54$, our late-time photometric limits are too shallow to place meaningful constraints on a potential SN component associated with GRB 230328B. The derived limiting absolute magnitude lies well above the peak luminosities of known GRB-associated SNe (S. O. Belkin et al. 2020; S. O. Belkin & A. S. Pozanenko 2024), therefore, these limits cannot be used to classify GRB 230328B as a genuinely SN-less event. The argument against such a classification thus rests entirely on the host galaxy properties described above. The high stellar mass and elevated SFR are instead consistent with a collapsar progenitor embedded in a massive, dusty galaxy where a contemporaneous SN could be substantially attenuated below the detection threshold at the observed redshift.

## 4 CONCLUSION

We present multiwavelength observations of GRB 230328B, spanning from 41 s post-trigger to deep host-galaxy imaging over a year later. This enables us to probe the physical mechanisms of the burst, characterize its environment, and place it within the broader population of long-duration GRBs. Our main findings are summarized below.

The prompt emission observed by *Fermi*/GBM shows a multi-pulsed light curve with $T_{90} = 21.6 \pm 0.4$ s. Spectral fitting with a cut-off power law yields peak energy $E_\mathrm{p} = 164^{+14}_{-12}$ keV. The long duration and soft spectrum classify it as a typical long GRB. Using the photometric redshift $z \approx 1.54$, we infer $E_\mathrm{iso} \approx 6.4 \times 10^{52}$ erg. In the rest frame, the burst is consistent with standard long-GRB correlations, including the Amati relation and the $T_{90,i}$–$EH$ diagram (Section 3.1).

Combined optical and X-ray modelling reveals significant line-of-sight absorption, with $A_V = 0.80 \pm 0.06$ mag. Broad-band fitting indicates that the host extinction is best described by MW or LMC-like curves rather than SMC-like dust. The high extinction suggests the burst occurred in or behind a dense star-forming region within the host galaxy, implying substantial intervening material along the line of sight (Section 3.3).

The optical and X-ray afterglow exhibits a complex morphology characterized by an onset bump and an achromatic optical rebrightening at about 4000 s. MCMC modelling reveals a highly relativistic and energetic initial blast wave with initial energy of $E_\mathrm{k,iso} \approx 8.3 \times 10^{53}$ erg. This corresponds to a radiative efficiency of $\approx 7$ per cent, which aligns with standard expectations for energy dissipation mechanisms in GRB jets. As the jet propagates through a low-density, weakly magnetized external medium, the late-time rebrightening can be explained by gradual energy injection from trailing shells. While this model reproduces the key afterglow features, the complexity of the multiparameter fit, early X-ray flaring, and a lack of contemporaneous early radio coverage introduce some uncertainties. Therefore, alternative physical scenarios, such as a structured two-component jet, cannot be ruled out (Section 3.4).

Based on observations taken 445 d after the burst, the host is identified as a relatively young S0-type galaxy at $z \approx 1.54$. Spanning approximately 30 kpc, it is comparable in size to the MW and resides in a complex environment, likely part of interacting galaxies. The burst afterglow was localized close (within 7 kpc) to this host galaxy centre. This central location, combined with the heavy dust absorption observed, strongly suggests that the event occurred deep within one of these highly obscured, active star-forming regions (Section 3.5).

We monitored the burst region from 3 to 48 d post-trigger to search for an associated SN, finding no variability or excess emission. At the estimated redshift $z \approx 1.54$, our limits are sensitive only to SNe brighter than typical GRB-associated events. Thus, any typical accompanying SN would be too faint to detect against the host galaxy background (Section 3.6).

Overall, GRB 230328B provides a valuable look at a massive stellar collapse within a dense, dusty galactic environment at $z \approx 1.54$. The complex behaviour of its afterglow and the strong dust absorption observed here underline the importance of future multiband observations. Observing GRBs rapidly across multiple wavelengths will be essential for separating the physics of the burst itself from the influence of its surrounding environment.

## ACKNOWLEDGEMENTS

We dedicate this work to the memory of Bruce Grossan, whose contributions were invaluable to this project.

We thank Bing Zhang for useful discussions. This research was funded by the Science Committee of the Ministry of Science and Higher Education of the Republic of Kazakhstan (Grant No. AP26103591). TK acknowledges support from Chinese National Foreign Expert Individual Project (Project No. 110000352520258002) and the CAS-ANSO Fellowship (Grant No. CAS-ANSO-FA-2024-06). EA was supported by the Nazarbayev University Faculty Development Competitive Research Grant Programme (no. 040225FD4713). MK was supported by the Science Committee of the Ministry of Science and Higher Education of the Republic of Kazakhstan (Grant No. BR21881880). RG was sponsored by the National Aeronautics and Space Administration (NASA) through a contract with ORAU. PB's work was funded by a NASA grant 80NSSC24K0770, a grant (no. 2020747) from the United States - Israel Binational Science Foundation (BSF), Jerusalem, Israel and by a grant (no. 1649/23) from the Israel Science Foundation. The NUTTELA-TAO Team expresses gratitude to the personnel of the Assy-Turgen Astrophysical Observatory and the Fesenkov Astrophysical Institute, Almaty, Kazakhstan, for their assistance. This work made use of data supplied by the UK *Swift* Science Data Centre at the University of Leicester.

AP, NP, AV, AM thank the RTTAC committee for providing time for observing on the BTA-6m and CMO-2.5m telescopes. EK is grateful to the Ministry of Science and Higher Education of the Russian Federation for financial support of this work; the AZT-33IK telescope is part of the Core Shared Research Facility 'Angara' of ISTP SB RAS. OAB and AP thank the Ministry of Higher Education, Science and Innovations of the Republic of Uzbekistan for its support, grant no. IL-5421101855. Observations of GRB 230328B were completed with the 22-meter radio telescope RT-22 of CrAO working at the frequency of 36.8 GHz using modulation radiometers (A.E. Volvach, L.N. Volvach, M.G. Larionov Characterizing Close Binary Supermassive Black Holes in Blazars 3C 273, 3C 454.3, S 0528+134, and AO 0235+164: Insights from Multi-Frequency Radio Monitoring and Gravitational Wave Prospects // The Astrophysical Journal, 2025. Vol.992, P.60. DOI: 10.3847/1538-4357/adfee2). The GROWTH India Telescope (GIT) is a 70-cm telescope with a 0.7° field of view, set up by the Indian Institute of Astrophysics (IIA) and the Indian Institute of Technology Bombay (IITB) with funding from Indo-US Science and Technology Forum and the Science and Engineering Research Board, Department of Science and Technology, Government of India. It is located at the Indian Astronomical Observatory (Hanle), operated by IIA. We acknowledge funding by the IITB alumni batch of 1994, which partially supports operations of the telescope. GCA acknowledges support from the Indian National Science Academy (INSA) under the INSA Senior Scientist programme.

## DATA AVAILABILITY

The data underlying this project are available from authors upon request.

## REFERENCES

Abbott B. P. et al., 2017, ApJ, 848, L13
Abdikamalov E., Beniamini P., 2025, MNRAS, 539, 2707
Abdullayev Z. et al., 2025, Rev. Mex. Astron. Astrofis, 59, 109,
Adami C. et al., 2023, GRB Coordinates Network, 33537, 1
Agui Fernandez J. F., de Ugarte Postigo A., Thoene C. C., Blazek M., Guijarro A., Cikota S., 2023, GRB Coordinates Network, 33549, 1
Aimuratov Y. et al., 2023, ApJ, 955, 93
Aimuratov Y. et al., 2025, Galaxies, 13 99
Akerlof C. et al., 1999, Nature, 398, 400
Akl D. et al., 2026, A&A, 710, A211
Amati L. et al., 2002, A&A, 390, 81
Angulo-Valdez C. et al., 2026, MNRAS, 546
Arnouts S., Cristiani S., Moscardini L., Matarrese S., Lucchin F., Fontana A., Giallongo E., 1999, MNRAS, 310, 540
Barkov M. V., Pozanenko A. S., 2011, MNRAS, 417, 2161
Becerra R. L. et al., 2021, ApJ, 908, 39
Becerra R. L. et al., 2023, MNRAS, 525, 3262
Belkin S. et al., 2023, GRB Coordinates Network, 33530, 1
Belkin S. O., Pozanenko A. S., 2024, Astron. Lett., 50, 701
Belkin S. O. et al., 2020, Astron. Lett., 46, 783
Beniamini P., Nakar E., 2019, MNRAS, 482, 5430
Beniamini P., Nava L., Piran T., 2016, MNRAS, 461, 51
Berger E. et al., 2003, Nature, 426, 154
Blackburn J. K., 1995, in Shaw R. A., Payne H. E., Hayes J. J. E. eds, ASP Conf. Ser. Vol. 77, Astronomical Data Analysis Software and Systems IV. Astron. Soc. Pac., San Francisco, p. 367
Blackburn J. K., Shaw R. A., Payne H. E., Hayes J. J. E., Heasarc, 1999, Astrophysics Source Code Library, record ascl:9912.002,
Bloom J. S., Kulkarni S. R., Djorgovski S. G., 2002, AJ, 123, 1111
Bloom J. S., Frail D. A., Kulkarni S. R., 2003, ApJ, 594, 674
Chambers K. C. et al., 2016, American Astronomical Society Meeting Abstracts, 231, 102.01
Cheng Y. et al., 2025, ApJ, 979, 38
Chevalier R. A., Li Z.-Y., 1999, ApJ, 520, L29
Clocchiatti A., Suntzeff N. B., Covarrubias R., Candia P., 2011, AJ, 141, 163
Covino S. et al., 2013, MNRAS, 432, 1231
Dainotti M. G. et al., 2024, MNRAS, 533, 4023
Dalessi S., Meegan C., Fermi GBM Team, 2023, GRB Coordinates Network, 33531, 1
de Wet S. et al., 2024, ApJ, 974, 279
Draine B. T., Hao L., 2002, ApJ, 569, 780
Elbaz D. et al., 2011, A&A, 533, A119
Fan Y., Piran T., 2006, MNRAS, 369, 197
Fermi GBM Team, 2023, GRB Coordinates Network, 33526, 1
Finneran G., Cotter L., Martin-Carrillo A., 2025, Astron. Comput., 52, 100954
Fioc M., Rocca-Volmerange B., 1997, A&A, 326, 950
Foreman-Mackey D., Hogg D. W., Lang D., Goodman J., 2013, PASP, 125, 306
Fraija N. et al., 2017, ApJ, 848, 15
Fu S.-Y. et al., 2026, preprint (arXiv:2604.14341)
Fynbo J. P. U. et al., 2006, Nature, 444, 1047
Galama T. J. et al., 1998, Nature, 395, 670
Gao H., Lei W.-H., Zou Y.-C., Wu X.-F., Zhang B., 2013, New Astron. Rev., 57, 141
Gehrels N. et al., 2006, Nature, 444, 1044
Gill R., Granot J., 2018, MNRAS, 478, 4128
Gill R., Granot J., 2023, MNRAS, 524, L78
Gill R. et al., 2026, preprint (arXiv:2605.26091)

Gompertz B. P., Malesani D. B., Levan A. J., 2023, GRB Coordinates Network, 33538, 1
Gorbovskoy E. S. et al., 2012, MNRAS, 421, 1874
Gordon K. D., 2024, J. Open Source Softw., 9, 7023
Graham J. F., Schady P., Fruchter A. S., 2023, ApJ, 954, 13
Greiner J. et al., 2024, A&A, 691, A158
Gropp J. D. et al., 2023, GRB Coordinates Network, 33527, 1
Grossan B., Kumar P., Smoot G. F., 2019, J. High Energy Astrophys., 23, 14
Gruber D. et al., 2014, ApJS, 211, 12
Gupta R. et al., 2021, MNRAS, 505, 4086
Gupta R. et al., 2022, J. Astrophys Astron., 43, 82
Gupta R., Bhushan Pandey S., Ror A. K., Aryan A., Nath Tiwari S., 2024, Bulletin de la Societe Royale des Sciences de Liege, 93, 683
Gupta R. et al., 2025, preprint (arXiv:2508.00142)
Gupta R. et al., 2026a, preprint (arXiv:2606.28267)
Gupta R. et al., 2026b, ApJ, 997, 246
Hjorth J. et al., 2003, Nature, 423, 847
Hu Y.-D. et al., 2021, A&A, 646, A50
Ilbert O. et al., 2006, A&A, 457, 841
Jelínek M. et al., 2025, A&A, 698, A162
Jia L.-W., Wu X.-F., Lü H.-J., Hou S.-J., Liang E.-W., 2012, Res. Astron. Astrophys., 12, 411
Kann D. A., Klose S., Zeh A., 2006, ApJ, 641, 993
Klotz A., Gendre B., Stratta G., Atteia J. L., Boër M., Malacrino F., Damerdji Y., Behrend R., 2006, A&A, 451, L39
Komesh T., Grossan B., Maksut Z., Abdikamalov E., Krugov M., Smoot G. F., 2023a, MNRAS, 520, 6104
Komesh T., Maksut Z., Grossan B., Abdullayev Z., Krugov M., Energetic Cosmos Laboratory, 2023b, GRB Coordinates Network, 33539, 1
Kouveliotou C., Meegan C. A., Fishman G. J., Bhat N. P., Briggs M. S., Koshut T. M., Paciesas W. S., Pendleton G. N., 1993, ApJ, 413, L101
Krühler T. et al., 2011, A&A, 534, A108
Krühler T. et al., 2015, A&A, 581, A125
Kugel F., Turpin D., Karpov S., Hussenot-Desenonges T., Antier S., Duverne P. A., Hello P., Klotz A., 2023, GRB Coordinates Network, 33550, 1
Kumar H. et al., 2022, AJ, 164, 90
Kumar P., Zhang B., 2015, Phys. Rep., 561, 1
Laskar T., Berger E., Margutti R., Perley D., Zauderer B. A., Sari R., Fong W.-f., 2015, ApJ, 814, 1
Laskar T. et al., 2018, ApJ, 859, 134
Lazzati D., Perna R., Flasher J., Dwarkadas V. V., Fiore F., 2006, MNRAS, 372, 1791
Li L. et al., 2012, ApJ, 758, 27
Li L., Wang Y., Shao L., Wu X.-F., Huang Y.-F., Zhang B., Ryde F., Yu H.-F., 2018, ApJS, 234, 26
Li L. et al., 2020, ApJ, 900, 176
Li Y., Li A., Wei D. M., 2008, ApJ, 678, 1136
Liang E.-W., Zhang B.-B., Zhang B., 2007, ApJ, 670, 565
Liang E.-W. et al., 2013, ApJ, 774, 13
Maksut Z., Grossan B., 2021, Rev. Mex. Astron. Astrofis., 53, 169
Markwardt C. B., et al., 2023, GRB Coordinates Network, 33541, 1.
Mazaeva E., Pozanenko A., Minaev P., 2018, Int. J. Mod. Phys. D, 27, 1844012
Mazets E. P. et al., 1981, Ap&SS, 80, 119
Meegan C. et al., 2009, ApJ, 702, 791
Melandri A. et al., 2017, A&A, 607, A29
Minaev P. Y., Pozanenko A. S., 2020a, Astron. Lett., 46, 573
Minaev P. Y., Pozanenko A. S., 2020b, MNRAS, 492, 1919
Minaev P. Y., Pozanenko A. S., 2021, MNRAS, 504, 926
Monet D. G. et al., 2003, AJ, 125, 984
Morgan A. N. et al., 2014, MNRAS, 440, 1810
Mukazhanov O., Abdikamalov E., Beniamini P., 2026, preprint (arXiv:2603.27225)
Nadjip A. E., Tatarnikov A. M., Toomey D. W., Shatsky N. I., Cherepashchuk A. M., Lamzin S. A., Belinski A. A., 2017, Astrophys. Bull., 72, 349
Nasa High Energy Astrophysics Science Archive Research Center (Heasarc), 2014, Astrophysics Source Code Library, record ascl:1408.004
National Optical Astronomy Observatories, The IRAF community, 2025, IRAF, Zenodo
Norris J. P., Bonnell J. T., Kazanas D., Scargle J. D., Hakkila J., Giblin T. W., 2005, ApJ, 627, 324
Nugent A. E. et al., 2022, ApJ, 940, 57
O'Connor B. et al., 2023, Sci. Adv., 9, eadi1405
Palmerio J. T. et al., 2019, A&A, 623, A26
Pandey S. B. et al., 2023, J. Astron. Instrum., 12, 2240009
Pankov N., Elenin L., Krylov A., Pozanenko A., Belkin S., IKI FuN G., 2023, GRB Coordinates Network, 33559, 1
Pei Y. C., 1992, ApJ, 395, 130
Peng F., Königl A., Granot J., 2005, ApJ, 626, 966
Perna R., Lazzati D., Fiore F., 2003, ApJ, 585, 775
Piran T., 1999, Phys. Rep., 314, 575
Poolakkil S. et al., 2021, ApJ, 913, 60
Pozanenko A. S., Barkov M. V., Minaev P. Y., Volnova A. A., 2021, Astron. Lett., 47, 791
Racusin J. L. et al., 2008, Nature, 455, 183
Ror A. K. et al., 2023a, ApJ, 942, 34
Ror A. K., Gupta R., Pandey S. B., Ghosh A., Aryan A., Misra K., 2023b, GRB Coordinates Network, 33547, 1
Rossi A., Maiorano E., Palazzi E., CIBO Collaboration, 2023, GRB Coordinates Network, 34141, 1
Rykoff E. S. et al., 2009, ApJ, 702, 489
Sari R., Mészáros P., 2000, ApJ, 535, L33
Sari R., Piran T., 1995, ApJ, 455, L143
Sari R., Piran T., 1999, ApJ, 520, 641
Savaglio S., Glazebrook K., Le Borgne D., 2006, in Holt S. S., Gehrels N., Nousek J. A. eds, AIP Conf. Proc. Vol. 836, Gamma-Ray Bursts in the Swift Era. Am. Inst. Phys., New York, p. 540
Savaglio S., Glazebrook K., Le Borgne D., 2009, ApJ, 691, 182
Schady P. et al., 2010, MNRAS, 401, 2773
Schlafly E. F., Finkbeiner D. P., 2011, ApJ, 737, 103
Schroeder G. et al., 2024, ApJ, 970, 139
Schroeder G. et al., 2025, ApJ, 982, 42
Seaton M. J., 1979, MNRAS, 187, 73
Sironi L., Spitkovsky A., 2011, ApJ, 726, 75
Taggart K., Perley D. A., 2021, MNRAS, 503, 3931
Tatarnikov A. M., Zheltoukhov S. G., Shatsky N. I., Burlak M. A., Maslennikova N. A., Vakhonin A. A., 2023, Astrophys. Bull., 78, 384
Tian X., Qin Y., Du M., Yi S.-X., Tang Y.-K., 2022, ApJ, 925, 54
Troja E. et al., 2022, Nature, 612, 228
Uhm Z. L., Zhang B., Hascoët R., Daigne F., Mochkovitch R., Park I. H., 2012, ApJ, 761, 147
Vestrand W. T. et al., 2005, Nature, 435, 178
Volnova A., Pozanenko A., Mazaeva E., Belkin S., Molotov I., Elenin L., Namkhai T., Buckley D., 2021, Anais da Academia Brasileira de Ciências, 93, e20200883
Volnova A. A. et al., 2014, MNRAS, 442, 2586
Volvach A., Nesterov N., Petrov L., 2000, Kinematika i Fizika Nebesnykh Tel Supplement, 3, 43
Volvach A. E., Volvach L. N., Strepka I. D., 2012, in IEEE, p. 36
Wang X.-G. et al., 2015, ApJS, 219, 9
Wilms J., Allen A., McCray R., 2000, ApJ, 542, 914
Woosley S. E., 1993, in AAS Meeting Abstracts #182. p. 55.05
Wright E. L., 2006, PASP, 118, 1711
Xin L. et al., 2023, Nat. Astron., 7, 724
Yi S.-X., Wu X.-F., Dai Z.-G., 2013, ApJ, 776, 120
Zhang B., 2006, Nature, 444, 1010
Zhang B., 2025, J. High Energy Astrophys., 45, 325
Zhang B., Mészáros P., 2002, ApJ, 566, 712
Zhang B. et al., 2009, ApJ, 703, 1696
Zhang B., Wang X.-Y., Zheng J.-H., 2024, J. High Energy Astrophys., 41, 42

## APPENDIX A: ADDITIONAL FIGURE AND TABLES

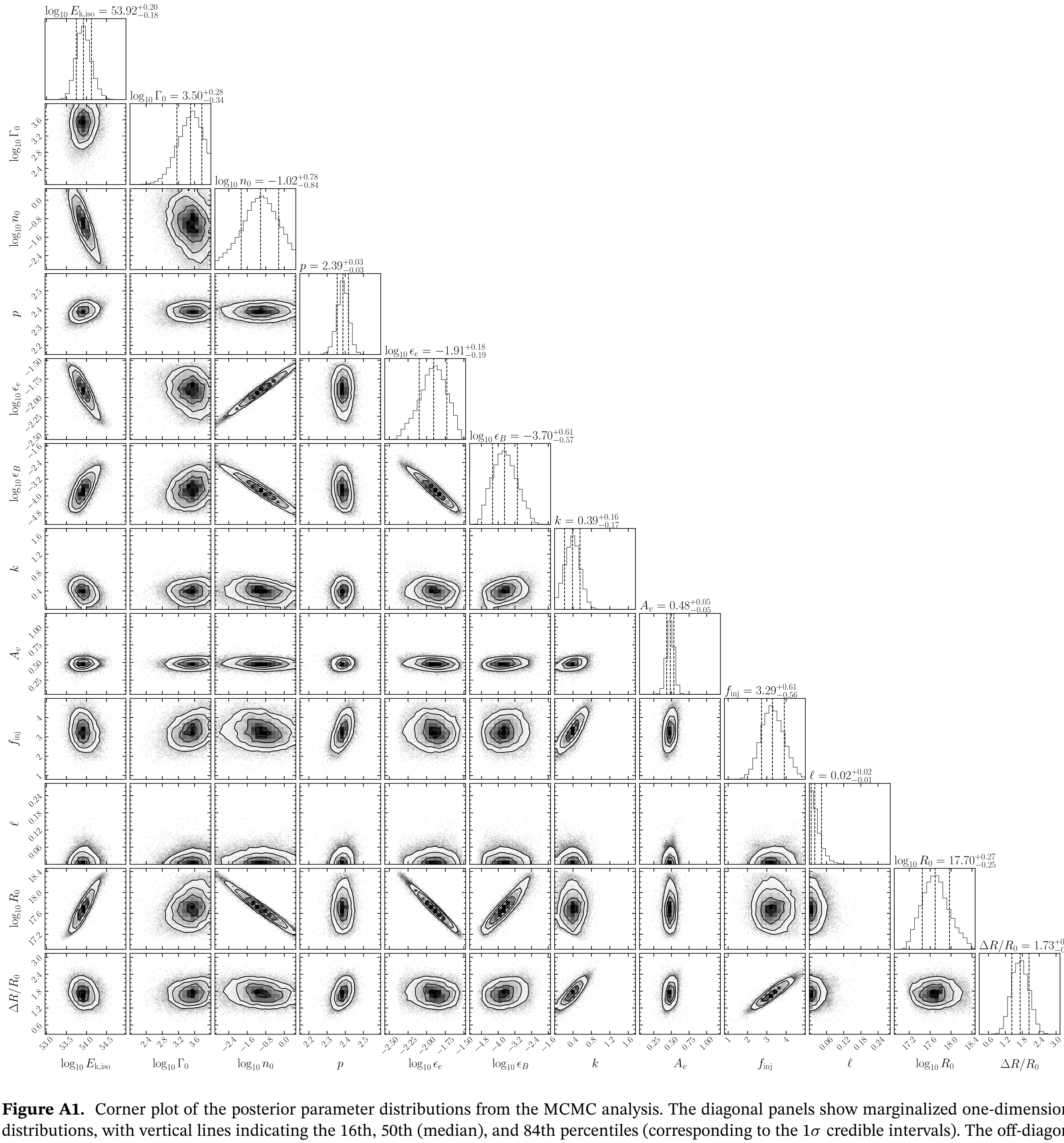


**Figure A1.** Corner plot of the posterior parameter distributions from the MCMC analysis. The diagonal panels show marginalized one-dimensional distributions, with vertical lines indicating the 16th, 50th (median), and 84th percentiles (corresponding to the $1\sigma$ credible intervals). The off-diagonal panels display two-dimensional joint constraints with density contours.

**Table A1.** NUTTELA-TAO observations. $t_{\rm mid}$ is the mid-point time of each co-add, and $t_0$ is the BAT trigger time, which occurred at 14:54:48 UT on 2023 March 28 (J. D. Gropp et al. 2023). $T_{\rm exp}$ denotes the exposure time of each image. The Milky Way extinction is subtracted.

| $t_{\rm mid} - t_0$ (s) | $T_{\rm exp}$ (s) | $g'$ filter | | $r'$ filter | | $i'$ filter | |
|---|---|---|---|---|---|---|---|
| | | mag (err) | Flux (err) (mJy) | mag (err) | Flux (err) (mJy) | mag (err) | Flux (err) (mJy) |
| 48 | 15 | 17.25 (0.13) | 0.457 (0.056) | 16.81 (0.08) | 0.683 (0.047) | 16.08 (0.09) | 1.338 (0.107) |
| 63 | 15 | 16.90 (0.10) | 0.633 (0.056) | 16.70 (0.07) | 0.760 (0.046) | 15.96 (0.08) | 1.494 (0.112) |
| 82 | 22 | 17.05 (0.12) | 0.550 (0.060) | 16.56 (0.05) | 0.861 (0.042) | 16.12 (0.08) | 1.298 (0.091) |
| 143 | 60 | 17.25 (0.09) | 0.455 (0.037) | 16.78 (0.04) | 0.706 (0.024) | 16.26 (0.06) | 1.139 (0.066) |
| 203 | 60 | 17.51 (0.13) | 0.360 (0.042) | 16.96 (0.04) | 0.599 (0.024) | 16.62 (0.07) | 0.815 (0.053) |
| 263 | 60 | 17.73 (0.11) | 0.294 (0.029) | 17.29 (0.06) | 0.440 (0.022) | 16.97 (0.08) | 0.593 (0.043) |
| 323 | 60 | 18.09 (0.14) | 0.211 (0.027) | 17.61 (0.08) | 0.328 (0.023) | 17.08 (0.08) | 0.536 (0.041) |
| 383 | 60 | 18.19 (0.15) | 0.192 (0.027) | 17.59 (0.08) | 0.334 (0.023) | 17.38 (0.10) | 0.406 (0.038) |
| 488 | 150 | 18.34 (0.10) | 0.167 (0.015) | 17.91 (0.06) | 0.248 (0.015) | 17.44 (0.08) | 0.382 (0.027) |
| 638 | 150 | 18.96 (0.17) | 0.094 (0.014) | 18.30 (0.09) | 0.174 (0.014) | 17.60 (0.08) | 0.332 (0.025) |
| 788 | 150 | 18.92 (0.15) | 0.098 (0.014) | 18.50 (0.13) | 0.144 (0.017) | 17.84 (0.10) | 0.265 (0.024) |
| 938 | 150 | 19.02 (0.16) | 0.090 (0.014) | 18.60 (0.20) | 0.132 (0.025) | 17.92 (0.10) | 0.246 (0.023) |
| 1163 | 300 | 19.35 (0.16) | 0.066 (0.010) | 18.84 (0.11) | 0.106 (0.011) | 18.00 (0.09) | 0.229 (0.019) |
| 1463 | 300 | 19.62 (0.18) | 0.051 (0.009) | 19.12 (0.19) | 0.081 (0.014) | 18.27 (0.11) | 0.179 (0.017) |
| 2304 | 600 | 19.37 (0.09) | 0.065 (0.006) | 19.36 (0.10) | 0.066 (0.006) | 18.69 (0.13) | 0.122 (0.014) |
| 2904 | 600 | 19.83 (0.14) | 0.042 (0.005) | 19.22 (0.09) | 0.074 (0.006) | 18.54 (0.10) | 0.139 (0.013) |
| 3504 | 600 | 19.57 (0.10) | 0.054 (0.005) | 19.14 (0.08) | 0.080 (0.006) | 18.52 (0.10) | 0.142 (0.013) |
| 4104 | 600 | 19.21 (0.07) | 0.075 (0.005) | 19.07 (0.08) | 0.085 (0.006) | 18.52 (0.08) | 0.142 (0.010) |
| 4704 | 600 | 19.57 (0.10) | 0.054 (0.005) | 19.29 (0.10) | 0.070 (0.006) | 18.48 (0.06) | 0.147 (0.008) |
| 5640 | 600 | 19.38 (0.09) | 0.064 (0.005) | 19.28 (0.09) | 0.070 (0.006) | 18.46 (0.06) | 0.151 (0.008) |
| 6420 | 600 | 19.20 (0.09) | 0.076 (0.006) | 19.44 (0.11) | 0.061 (0.006) | 18.32 (0.13) | 0.171 (0.021) |

*Note.* Calibration procedures involved referencing four bright stars from the Pan-STARRS catalogue within our images with object IDs: 204052911191064516, 203992906791944462, 204042913023972808, and 204042912675745804.

**Table A2.** Later observations. $t_{mid}$ is the mid-point time of each co-add, and $t_0$ is the BAT trigger time, which occurred at 14:54:48 UT on 2023 March 28 (J. D. Gropp et al. 2023). $T_{exp}$ denotes the exposure time of each image. The Milky Way extinction is subtracted.

| Date | Site/Instrument | Band | $t_{mid} - t_0$ (s) | $T_{exp}$ (s) | mag (err) | Flux (err) (mJy) | References |
|---|---|---|---|---|---|---|---|
| 2023-03-28 | Mondy/AZT-33IK | *R* | 2251 | 600.0 | 19.38 (0.07) | 0.064 (0.004) | This work |
| 2023-03-28 | Mondy/AZT-33IK | *R* | 2852 | 600.0 | 19.45 (0.08) | 0.060 (0.005) | This work |
| 2023-03-28 | Mondy/AZT-33IK | *R* | 3452 | 600.0 | 19.29 (0.09) | 0.070 (0.006) | This work |
| 2023-03-28 | Mondy/AZT-33IK | *R* | 4053 | 600.0 | 19.39 (0.10) | 0.064 (0.006) | This work |
| 2023-03-28 | Mondy/AZT-33IK | *R* | 4653 | 600.0 | 19.38 (0.09) | 0.064 (0.006) | This work |
| 2023-03-28 | Mondy/AZT-33IK | *R* | 5373 | 600.0 | 19.38 (0.07) | 0.064 (0.004) | This work |
| 2023-03-28 | Mondy/AZT-33IK | *R* | 5975 | 600.0 | 19.48 (0.06) | 0.058 (0.003) | This work |
| 2023-03-28 | Mondy/AZT-33IK | *R* | 6575 | 600.0 | 19.45 (0.06) | 0.060 (0.004) | This work |
| 2023-03-28 | Mondy/AZT-33IK | *R* | 7176 | 600.0 | 19.50 (0.06) | 0.058 (0.004) | This work |
| 2023-03-28 | Mondy/AZT-33IK | *R* | 7776 | 600.0 | 19.45 (0.06) | 0.060 (0.004) | This work |
| 2023-03-28 | Mondy/AZT-33IK | *R* | 8377 | 600.0 | 19.61 (0.06) | 0.052 (0.003) | This work |
| 2023-03-28 | Mondy/AZT-33IK | *R* | 8977 | 600.0 | 19.83 (0.07) | 0.043 (0.003) | This work |
| 2023-03-28 | Mondy/AZT-33IK | *R* | 18521 | 3480.0 | 20.33 (0.09) | 0.026 (0.002) | This work |
| 2023-03-29 | Mondy/AZT-33IK | *R* | 88340 | 3600 | 21.81 (0.09) | 0.007 (0.001) | This work |
| 2023-04-05 | Mondy/AZT-33IK | *R* | 693297 | 7200 | >22.5 | <0.004 | This work |
| 2023-04-11 | Mondy/AZT-33IK | *R* | 1225109 | 7200 | 23.07 (0.21) | 0.002 (0.001) | This work |
| 2023-04-13 | Mondy/AZT-33IK | *R* | 1395378 | 7080 | 23.43 (0.58) | 0.002 (0.001) | This work |
| 2023-04-14 | Mondy/AZT-33IK | *R* | 1472671 | 8400 | 23.03 (0.20) | 0.002 (0.001) | This work |
| 2023-04-22 | Mondy/AZT-33IK | *R* | 2213162 | 10800 | 23.05 (0.11) | 0.002 (0.001) | This work |
| 2023-03-28 | ISON-Multa/Santel-400 | *Clear* | 3977 | 5400 | 18.87 (0.13) | 0.103 (0.011) | This work |
| 2023-03-28 | ISON-Kitab/RC-36 | *Clear* | 3658 | 1140 | >17.6 | <0.330 | This work |
| 2023-03-28 | IAO/GIT | *r* | 8638 | 1800 | 19.30 (0.13) | 0.068 (0.008) | This work |
| 2023-03-28 | IAO/GIT | *r* | 13064 | 1500 | 19.93 (0.15) | 0.038 (0.005) | This work |
| 2023-03-28 | IAO/GIT | *r* | 25926 | 600 | 20.23 (0.18) | 0.029 (0.005) | This work |
| 2023-03-28 | IAO/GIT | *g* | 8636 | 1200 | 19.64 (0.12) | 0.050 (0.005) | This work |
| 2023-03-28 | IAO/GIT | *g* | 25254 | 600 | 21.01 (0.35) | 0.014 (0.004) | This work |
| 2023-03-28 | IAO/GIT | *i* | 9954 | 1200 | 19.49 (0.23) | 0.057 (0.012) | This work |
| 2023-03-28 | IAO/GIT | *i* | 26581 | 600 | 19.96 (0.20) | 0.037 (0.007) | This work |
| 2023-03-28 | AbAO/AS-32 | *R* | 7493 | 6240 | 19.48 (0.10) | 0.059 (0.006) | This work |
| 2023-03-28 | UAFO/RC-500 | *Clear* | 8408 | 4050 | 19.32 (0.15) | 0.068 (0.009) | This work |
| 2023-03-28 | ARIES/DOT | *R* | 25026 | 300 | 20.46 (0.03) | 0.024 (0.001) | This work |
| 2023-03-28 | ARIES/DOT | *R* | 25566 | 300 | 20.57 (0.04) | 0.021 (0.001) | This work |
| 2023-03-28 | ARIES/DOT | *R* | 25876 | 300 | 20.48 (0.03) | 0.023 (0.001) | This work |
| 2023-03-28 | ARIES/DOT | *R* | 28423 | 300 | 20.56 (0.03) | 0.022 (0.001) | This work |
| 2023-03-28 | ARIES/DOT | *R* | 28734 | 300 | 20.57 (0.05) | 0.021 (0.001) | This work |
| 2023-03-28 | ARIES/DOT | *R* | 29044 | 300 | 20.61 (0.04) | 0.021 (0.001) | This work |
| 2023-03-29 | ARIES/DOT | *R* | 107600 | 300 | 22.04 (0.05) | 0.005 (0.001) | This work |
| 2023-04-15 | ORM/GTC | *r* | 1518033 | 60 | 23.70 (0.25) | 0.001 (0.000) | This work |
| 2023-04-15 | SAO/BTA | *g* | 1581153 | 600 | 23.56 (0.13) | 0.001 (0.001) | This work |
| 2023-05-15 | SAO/BTA | *g* | 4184745 | 2280 | 23.37 (0.04) | 0.001 (0.001) | This work |
| 2023-04-15 | SAO/BTA | *r* | 1583148 | 700 | 23.09 (0.10) | 0.002 (0.001) | This work |
| 2023-05-14 | SAO/BTA | *r* | 4094954 | 2400 | 23.02 (0.04) | 0.002 (0.001) | This work |
| 2023-04-15 | SAO/BTA | *i* | 1581129 | 1200 | 22.85 (0.10) | 0.003 (0.001) | This work |
| 2023-05-15 | SAO/BTA | *i* | 4188717 | 3960 | 22.88 (0.04) | 0.003 (0.001) | This work |
| 2023-04-23 | CrAO/ZTSh | *R* | 2275085 | 7440 | 23.47 (0.27) | 0.001 (0.001) | This work |
| 2023-05-13 | MAO/AZT-22 | *I* | 4000776 | 3600 | 22.85 (0.27) | 0.001 (0.001) | This work |
| 2023-05-19 | MAO/AZT-22 | *R* | 4517448 | 3600 | 23.19 (0.35) | 0.002 (0.001) | This work |
| 2023-03-30 | CrAO/RT-22 | 36.8 GHz | 152172 | 12180 | – | 2.3 (1.2) | This work |
| 2023-03-31 | CrAO/RT-22 | 36.8 GHz | 239172 | 9360 | – | 2.8 (1.2) | This work |
| 2023-04-01 | CrAO/RT-22 | 36.8 GHz | 329172 | 11400 | – | 3.4 (1.3) | This work |
| 2023-04-02 | CrAO/RT-22 | 36.8 GHz | 418032 | 9960 | – | 3.3 (1.1) | This work |
| 2023-04-03 | CrAO/RT-22 | 36.8 GHz | 505692 | 9000 | – | 3.2 (1.1) | This work |
| 2023-04-04 | CrAO/RT-22 | 36.8 GHz | 591372 | 5820 | – | 2.6 (1.2) | This work |
| 2023-04-05 | CrAO/RT-22 | 36.8 GHz | 680772 | 5820 | – | 1.8 (1.2) | This work |
| 2023-03-28 | *Swift*/UVOT | *white* | 188 | 147 | – | 0.075 (0.003) | This work |
| 2023-03-28 | *Swift*/UVOT | *white* | 5635 | 196 | – | 0.015 (0.001) | This work |
| 2023-03-28 | *Swift*/UVOT | *u* | 451 | 246 | – | 0.034 (0.005) | This work |
| 2023-03-28 | *Swift*/UVOT | *u* | 5226 | 246 | – | 0.015 (0.004) | This work |
| 2023-03-28 | *Swift*/UVOT | *v* | 99 | 246 | – | 0.322 (0.113) | This work |
| 2023-03-28 | *Swift*/UVOT | *v* | 4611 | 246 | – | 0.040 (0.016) | This work |
| 2023-03-28 | *Swift*/UVOT | *b* | 5431 | 246 | – | 0.029 (0.007) | This work |
| 2023-03-28 | OHP/T120 | $R_c$ | 16200 | 3000 | 20.08 (0.10) | 0.033 (0.003) | C. Adami et al. (2023) |

**Table A2** – *continued*

| Date | Site/Instrument | Band | $t_{\mathrm{mid}} - t_0$ (s) | $T_{\mathrm{exp}}$ (s) | mag (err) | Flux (err) (mJy) | References |
|---|---|---|---|---|---|---|---|
| 2023-03-28 | GRANDMA/KNC | $R_{\mathrm{c}}$ | 19157 | 2160 | 20.24 (0.10) | 0.029 (0.003) | F. Kugel et al. (2023) |
| 2023-03-28 | CAHA/CAFOS | $R_{\mathrm{c}}$ | 40754 | 1800 | 20.84 (0.06) | 0.016 (0.003) | J. F. Agui Fernandez et al. (2023) |
| 2023-03-28 | ORM/Liverpool | $i'$ | 44640 | 1800 | 20.63 (0.07) | 0.020 (0.001) | B. P. Gompertz, D. B. Malesani & A. J. Levan (2023) |
| 2023-03-28 | ORM/Liverpool | $r'$ | 44640 | 1800 | 21.00 (0.06) | 0.014 (0.001) | B. P. Gompertz et al. (2023) |

[1]*Energetic Cosmos Laboratory, Nazarbayev University, Astana 010000, Kazakhstan*
[2]*State Key Laboratory of Radio Astronomy and Technology, Xinjiang Astronomical Observatory, CAS, 150 Science 1Street, Urumqi, Xinjiang 830011, China*
[3]*Institute of Experimental and Theoretical Physics, Al-Farabi Kazakh National University, Almaty 050040, Kazakhstan*
[4]*Space Research Institute, Russian Academy of Sciences, Moscow 117997, Russia*
[5]*Faculty of Physics, Higher School of Economics, Moscow 101000, Russia*
[6]*Instituto de Radioastronomía y Astrofísica, Universidad Nacional Autónoma de México, Antigua Carretera a Pátzcuaro #8701, Ex-Hda. San José de la Huerta, Morelia, Michoacán, C.P. 58089, México*
[7]*Astrophysics Research Center of the Open University (ARCO), The Open University of Israel, PO Box 808, Ra'anana 4353701, Israel*
[8]*Space Sciences Laboratory, University of California, Berkeley, CA 94720, USA*
[9]*National Astronomical Observatories, Chinese Academy of Sciences, Beijing 100101, China*
[10]*University of Chinese Academy of Sciences, Beijing 100080, China*
[11]*School of Physics & Astronomy, Monash University, Clayton VIC 3800, Australia*
[12]*Fesenkov Astrophysical Institute, Almaty 050020, Kazakhstan*
[13]*Special Astrophysical Observatory, Russian Academy of Sciences, Nizhny Arkhyz 369167, Russia*
[14]*Department of Physics, Nazarbayev University, 53 Kabanbay Batyr Ave, Astana 010000, Kazakhstan*
[15]*Institute of Solar-Terrestrial Physics, Russian Academy of Sciences (Siberian Branch), Irkutsk 664033, Russia*
[16]*Lomonosov Moscow State University, Moscow 119991, Russia*
[17]*Crimean Astrophysical Observatory, Russian Academy of Sciences, Nauchny 298409, Crimea*
[18]*Ulugh Beg Astronomical Institute, Uzbekistan Academy of Sciences, Tashkent 100052, Uzbekistan*
[19]*Samarkand State University, 15, University Boulevard, Samarkand 140104, Uzbekistan*
[20]*Evgeni Kharadze Georgian National Astrophysical Observatory, Abastumani-Kanobili 0301, Georgia*
[21]*Samtskhe-Javakheti State University, Akhaltsikhe 0080, Georgia*
[22]*Keldysh Institute of Applied Mathematics of the Russian Academy of Sciences, Moscow 125047, Russia*
[23]*Institute of Applied Astronomy of Russian Academy of Science, 10 Kutuzova Emb., Saint-Petersburg 191187, Russia*
[24]*Aryabhatta Research Institute of Observational Sciences (ARIES), Manora Peak, Nainital, Uttarakhand 263001, India*
[25]*Astrophysics Science Division, NASA Goddard Space Flight Center, Mail Code 661, Greenbelt, MD 20771, USA*
[26]*Department of Physics, Indian Institute of Technology Bombay, Powai 400 076, India*
[27]*Indian Institute of Astrophysics, 2nd Block 100 Feet Rd, Koramangala Bangalore 560 034, India*
[28]*Instituto de Astrofísica de Andalucía – CSIC, Glorieta de la Astronomía s/n, E-18008 Granada, Spain*
[29]*Université de la Côte d'Azur, Nice, France*
[30]*IJCLab, Univ Paris-Saclay, CNRS/IN2P3, Orsay, France*
[31]*Department of Natural Sciences, The Open University of Israel, PO Box 808, Ra'anana 4353701, Israel*
[32]*Department of Physics, The George Washington University, 725 21st Street NW, Washington, DC 20052, USA*

This paper has been typeset from a TEX/LATEX file prepared by the author.